Award Number:
W81XWH-07-1-0708

TITLE:
Design, Fabrication, Characterization and Modeling of Integrated Functional Materials

PRINCIPAL INVESTIGATOR:
PI: Pritish Mukherjee, Ph.D.
Co-PIs: Hariharan Srikanth, Ph.D.
Sarath Witanachchi, Ph.D.
George Nolas, Ph.D.

CONTRACTING ORGANIZATION:
University of South Florida
4202 East Fowler Avenue
Tampa, FL 33620, USA

REPORT DATE:
October 2008

TYPE OF
REPORT: Annual

PREPARED FOR: U.S. Army Medical Research and Materiel Command
Fort Detrick, Maryland 21702-5012

DISTRIBUTION STATEMENT:

X Approved for public release; distribution unlimited

The views, opinions and/or findings contained in this report are those of the author(s) and should not be construed as an official Department of the Army position, policy or decision unless so designated by other documentation.

REPORT DOCUMENTATION PAGE

Form Approved
OMB No. 0704-0188

Public reporting burden for this collection of information is estimated to average 1 hour per response, including the time for reviewing instructions, searching existing data sources, gathering and maintaining the data needed, and completing and reviewing this collection of information. Send comments regarding this burden estimate or any other aspect of this collection of information, including suggestions for reducing this burden to Department of Defense, Washington Headquarters Services, Directorate for Information Operations and Reports (0704-0188), 1215 Jefferson Davis Highway, Suite 1204, Arlington, VA 22202-4302. Respondents should be aware that notwithstanding any other provision of law, no person shall be subject to any penalty for failing to comply with a collection of information if it does not display a currently valid OMB control number. **PLEASE DO NOT RETURN YOUR FORM TO THE ABOVE ADDRESS.**

1. REPORT DATE	2. REPORT TYPE	3. DATES COVERED
(19-10-2008)	Annual	*20 Sep 2007-19 Sep 2008*

4. TITLE AND SUBTITLE
Design, Fabrication, Characterization and Modeling of Integrated Functional Materials

5a. CONTRACT NUMBER
W81XWH-07-1-0708

5b. GRANT NUMBER

5c. PROGRAM ELEMENT NUMBER

6. AUTHOR(S)
PI: British Mukherjee, Ph.D.
co-PIs: Hariharan Srikanth, Ph.D.; Sarath Witanachchi, Ph. D.; George Nolas, Ph.D.

5d. PROJECT NUMBER

5e. TASK NUMBER

5f. WORK UNIT NUMBER

7. PERFORMING ORGANIZATION NAME(S) AND ADDRESS(ES)
University of South Florida
4202 East Fowler Avenue
Tampa, FL 33620, USA

8. PERFORMING ORGANIZATION REPORT NUMBER

9. SPONSORING / MONITORING AGENCY NAME(S) AND ADDRESS(ES)
U.S. Army Medical Research and Materiel Command
Fort Detrick, Maryland 21702-5012

10. SPONSOR/MONITOR'S ACRONYM(S)

11. SPONSOR/MONITOR'S REPORT NUMBER(S)

12. DISTRIBUTION / AVAILABILITY STATEMENT
Approved for public release; distribution unlimited

13. SUPPLEMENTARY NOTES

14. ABSTRACT
The dynamically evolving needs of the U.S. soldier in the battlefield in response to changes in the technology of warfare and associated threats require advances in multiple areas including biomedical diagnostics, chemical sensing, communication technology, efficient power generation without increased payload, and mobile refrigeration. These technological advances are critically dependent on the development of new and currently non-existing materials. This research addresses the directed development of novel materials towards long-term needs of the United States Army. In order to address specific areas of integrated functional materials targeted towards the needs of the U.S. soldier in the field we have initiated research efforts in three main areas which are diagnostics and sensing, communication and energy, and power generation and refrigeration. The specific three independent "Tasks" that have been undertaken are:
Task I: Nanostructured materials for biomedical diagnostics and chemical sensing
Task II: Multifunctional composites for communication and energy applications
Task III: Solid-state materials for power generation and refrigeration
The specific outcome of the research activities is expected to lead to new devices/systems/composite materials useful for the USAMRMC.

15. SUBJECT TERMS
Functional materials, integrated fabrication, nanobiotechnology, smart materials, multifunctional, dimensional integration, nanocomposites, sensor technology, thermoelectrics, solar cells, photovoltaics

16. SECURITY CLASSIFICATION OF:			17. LIMITATION OF ABSTRACT	18. NUMBER OF PAGES	19a. NAME OF RESPONSIBLE PERSON
a. REPORT	b. ABSTRACT	c. THIS PAGE			USAMRMC
U	U	U	UU	59	19b. TELEPHONE NUMBER *(include area code)*

Design, Fabrication, Characterization and Modeling of Integrated Functional Materials

(Program Director and PI: Prof. Pritish Mukherjee, Department of Physics, USF, Tampa, FL)
(co-PIs: Profs. Hariharan Srikanth, Sarath Witanachchi and George Nolas)

Table of Contents

Design, Fabrication, Characterization and Modeling of Integrated Functional Materials

(Program Director and PI: Prof. Pritish Mukherjee, Department of Physics, USF, Tampa, FL)
(co-PIs: Profs. Hariharan Srikanth, Sarath Witanachchi and George Nolas)

I. Introduction

The dynamically evolving needs of the U.S. soldier in the battlefield in response to changes in the technology of warfare and associated threats require advances in multiple areas including biomedical diagnostics, chemical sensing, communication technology, efficient power generation without increased payload, and mobile refrigeration. These technological advances are critically dependent on the development of new and currently non-existing materials. This research addresses the directed development of novel materials towards long-term needs of the United States Army.

Objective:

In addition to the integration of multiple functionalities with desirable properties (thermal, electrical, magnetic, mechanical, optical, etc.), the connection to real-world applications and devices also requires the seamless integration of dimensions (nano, micro, meso, macro) leading to integrated functional materials. We have initiated this Integrated Functional Materials Project at the Physics Department at the University of South Florida (USF) geared towards precisely addressing this grand challenge of dual integration. A series of targeted projects specifically address a spectrum of issues relevant to the needs of the U.S. soldier.

Specific Aims:

The Physics Department at the University of South Florida is home to a unique doctoral program in Applied Physics with an affiliated industrial practicum and nationally recognized research programs in physical and chemical materials synthesis and characterization of bulk materials, thin films and nanomaterials; crystal fiber growth; fundamentals of materials manufacturing processes and computational theoretical materials physics. This research synergistically coalesces existing expertise and leverages research infrastructure at USF in novel bulk materials synthesis, thin film growth, and nanotechnology. These goals are being further addressed through multidisciplinary research and new infrastructure development. The basic purpose of this project is to develop the novel science base both in the areas of multi-scale dimensional integration as well as multiple functional integration leading to previously unattained integrated functional materials.

Study Design:

In order to address specific areas of integrated functional materials targeted towards the needs of the U.S. soldier in the field we are directing the research efforts in three main areas which are diagnostics and sensing, communication and energy, and power generation and refrigeration. The specific three independent “Tasks”, further subdivided into seven “Projects” are:

Task I: Nanostructured materials for biomedical diagnostics and chemical sensing
(Technical Directors.: Drs. H. Srikanth and P. Mukherjee)

Project 1 Functional magnetic fluids for biomedical applications

Project 2 Nanoporous/nano-wire structures and polymer nanotemplates for sensing and molecular manipulation

Project 3 Carbon-nanotube based sensors

Project 4 Functional materials for affecting cell proliferation and locomotion

Task II: Multifunctional composites for communication and energy applications
(Technical Director: Dr. S. Witanachchi)

Project 5 Tunable multifunctional nano- and heterostructures for RF and microwave applications

Project 6 Flexible photonic materials for solar-based energy sources

Task III: Solid-state materials for power generation and refrigeration
(Technical Director: Dr. G. S. Nolas)

Project 7 High-performance nanofabricated thermoelectric materials for power generation and refrigeration

The timeline for proposed activities for each of these projects (over the three-year period of research) is detailed in the Gantt chart on the following page.

		Start Date	Duration	End date
1	**Project 1: Functional magnetic fluids for biomedical applications**			
1.1	Synthesis of magnetic nanoparticles & ferrofluids	09/01/07	365	08/31/08
1.2	Functionalization and characterization	01/01/08	365	12/31/08
1.3	Magnetic and hydrodynamic properties under flow	01/01/09	365	12/31/09
1.4	Fabrication of magnetic nanostructures for hyperthermia applications	09/01/09	365	08/31/10
2	**Project 2: Nanoporous/nanowire structures & polymer nanotemplates for sensing/molecular manipulation**			
2.1	Fabrication of In nano-pore structures and growth of nanowires of sensor materials	09/01/07	365	08/31/08
2.2	Molecular dynamic simulation of nanostructures	04/01/08	730	03/31/10
2.3	Formation of polymer nano-templates and manipulation of biomolecules	01/01/09	635	08/31/10
3	**Project 3: Carbon nanotube based sensors**			
3.1	Fabrication/characterization of C- nanotube networks	09/01/07	365	08/31/08
3.2	Modeling of biosensors for toxic adsorption	04/01/08	730	03/31/10
3.3	Biosensor fabrication and study of surface adsorption	01/01/09	635	08/31/10
4	**Project 4: Functional materials for affecting cell proliferation and locomotion**			
4.1	Study frequency-dependent cell growth	09/01/07	365	08/31/08
4.2	Study cell locomotion in electric fields	09/01/08	180	3/31/209
4.3	Study cell adhesion and migration on nanopatterned substrates	04/01/09	365	03/31/10
4.4	Fabrication of functional materials for cell sorting	09/01/09	365	08/31/10
5	**Project 5: Tunable multifunctional nano- and heterostructures for high frequency applications**			
5.1	Synthesis of ferrite nanoparticles and polymer nanocomposite films	09/01/07	365	08/31/08
5.2	Growth/characterization of ferromagnetic /ferroelectric nano and heterostructures.	01/01/08	365	12/31/08
5.3	Fabrication of multiferroic devices	01/01/09	635	08/31/10
6	**Project 6: Flexible photonic materials for solar cell devices**			
6.1	Growth and characterization of quantum dot/polymer hybrid structures	09/01/07	730	08/31/09
6.2	Fabricate and evaluate tandem structures.	09/01/09	365	08/31/10
7	**Project 7: Solid-state materials for power generation and refregiration**			
7.1	Growth of nanocomposite thermoelectrics	09/01/07	365	08/31/08
7.2	Investigate thermoelectric core-shell nanocomposites	09/01/08	365	08/31/09
7.3	Design of prototype devices	09/01/09	365	08/31/10

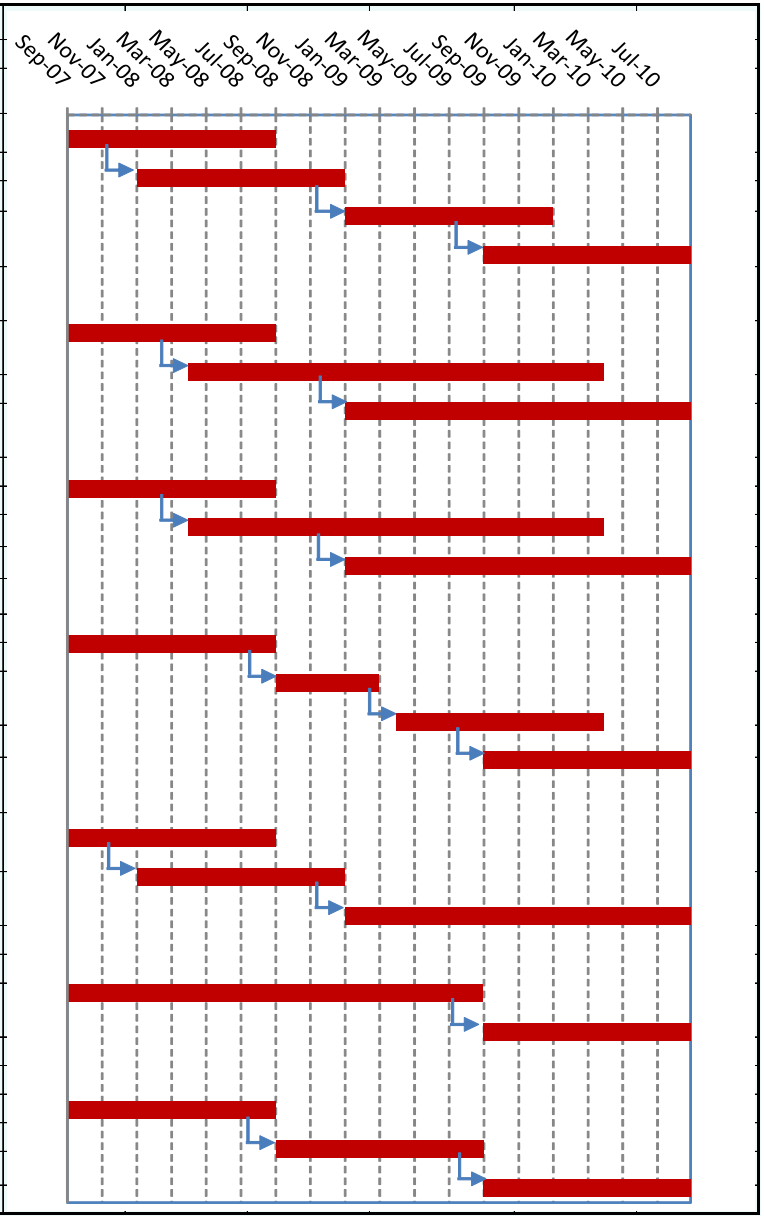

II. Technical Description of Research Progress

The following discussion details the progress made on each of the Tasks (by project) during the first year of research:

Task I: Nanostructured materials for biomedical diagnostics and chemical sensing

This task is divided into the following projects –
Project 1 – Functional magnetic fluids for biomedical applications
Project 2 - Nanoporous/nano-wire structures and polymer nanotemplates for sensing and molecular manipulation
Project 3 – Carbon-nanotube based sensors
Project 4 – Functional materials for affecting cell proliferation and locomotion

Project 1 – Functional magnetic fluids for biomedical applications: synthesis and magnetic properties of ferrofluids

The goal of this project is to synthesize and characterize ferrofluids that would serve as biocompatible carriers for targeted drug delivery. Ph.D. student Ms. Marienette Morales has been supported as a Graduate Research Assistant since January 2008. In addition, Master's student Ms. Melody Miner and undergraduate student Ms. Kristen Stojak assisted her during Summer 2008 with aspects of synthesis of nanoparticles. In February 2008, Dr. Susmita Pal was hired as a Postdoctoral Researcher in CIFM. Being a synthetic chemist, she has contributed to three projects in Task I. We continued our fundamental studies of the physical properties of various types of magnetic fluids during the year. Extensive experiments were conducted to characterize various types of nanoparticle loaded ferrofluids and correlate the microstructure with the magnetic response in these systems. A fundamental understanding of the relaxation mechanisms in these ferrofluids is very important for their eventual use in biomedical applications.

Magnetic properties of ferrofluids:

Ferrofluids are technologically important for a variety of applications ranging from biomedicine, hydraulics to power generation [1]. They are also model systems for the investigation of the magnetic characteristics and relaxation phenomena in magnetic nanoparticles [1-9]. It has been shown that the magnetic properties of ferrofluids are dominated by the dipole-dipole interaction between the suspended particles [2]. Particle size distribution [3], concentration [4,5], and surfactant coating [6] as well as solvent used in the suspension [7] all affect the dipole-dipole interaction [2], which in turn give rise to the range in magnetic behavior observed [8,9]. In particular, the temperature-dependent complex susceptibility ($\chi=\chi'-i\chi''$) has been noted in earlier experiments to show two characteristic peaks [8] and the zero-field-cooled (ZFC) magnetization to exhibit glass-like cusp and magnetic anomaly [9].

We synthesized and conducted a systematic comparative study of the magnetization and relaxation mechanisms in Fe_3O_4 nanoparticles in two different carrier liquids –hexane and dodecane -having different viscosities. In addition to the different viscosities of the fluids providing different environments for dipole-dipole interactions and chain formations, the characteristic temperatures in these two cases are such that the nanoparticle blocking temperature

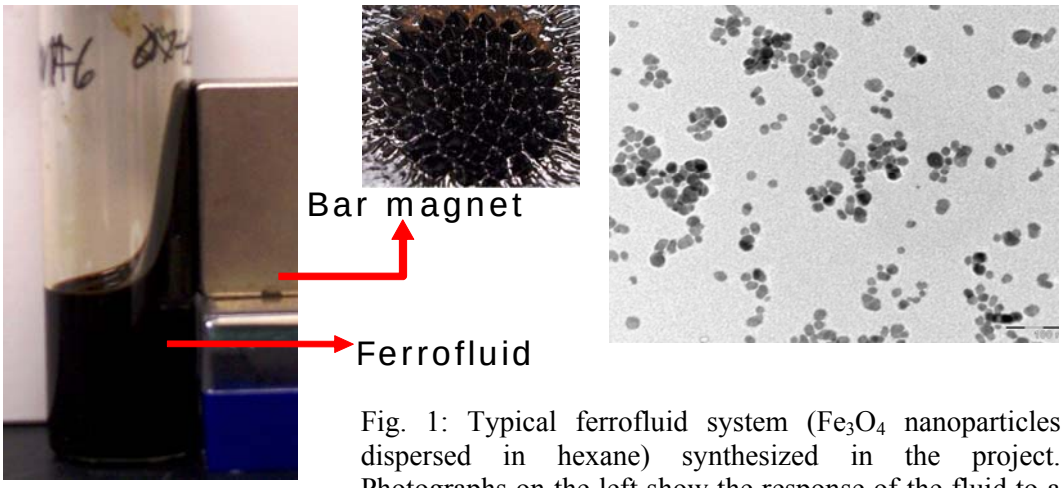

Fig. 1: Typical ferrofluid system (Fe_3O_4 nanoparticles dispersed in hexane) synthesized in the project. Photographs on the left show the response of the fluid to a bar magnet. TEM image of Fe_3O_4 nanoparticles (of mean size 14nm) used in the ferrofluids is also shown.

(~179K) is just above the freezing temperature of hexane (178 K) and much below the freezing temperature of dodecane (~264 K). Figure 1 shows a typical example system synthesized and investigated in this project.

Fe_3O_4 and $CoFe_2O_4$ nanoparticles were synthesized by chemical co-precipitation. The particles were washed several times with ethanol by magnetic decantation. We then dissolved a fixed amount of particles in hexane and dodecane and studied the magnetic properties of static ferrofluids, which are Fe_3O_4 and $CoFe_2O_4$ suspended in two different kinds of solvents, hexane and dodecane. The crystal structure and particle sizes were determined using a Bruker D8 Focus x-ray diffractometer (XRD) and a Morgagni 268D transmission electron microscope (TEM). The DC and AC magnetization measurements were done using a commercial Physical Property Measurement System (PPMS) available in our Functional Materials Laboratory.

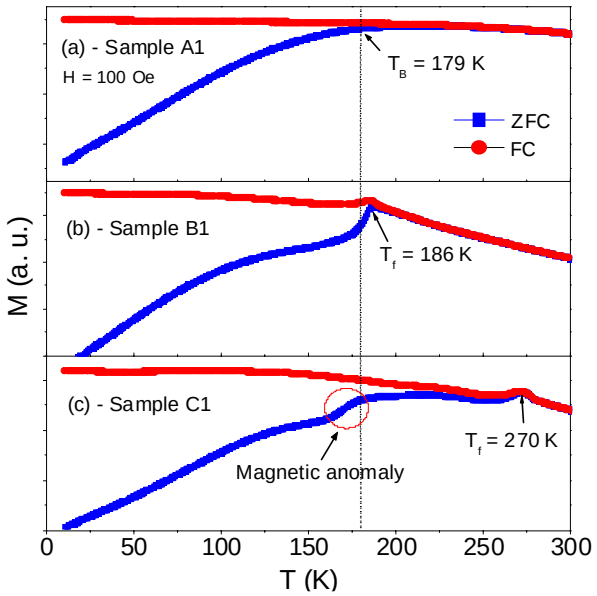

Fig. 2: ZFC-FC curves of Fe_3O_4 (a) dry powder (Sample A1), (b) dispersed in hexane (Sample B1) and (c) dispersed in dodecane (Sample C1).

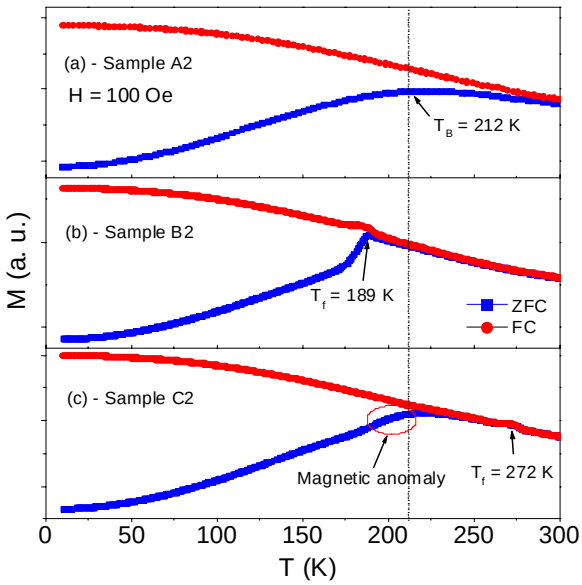

Fig. 3: ZFC-FC curves of $CoFe_2O_4$ (a) dry powder (Sample A2), (b) dispersed in hexane (Sample B2) and (c) dispersed in dodecane (Sample C2).

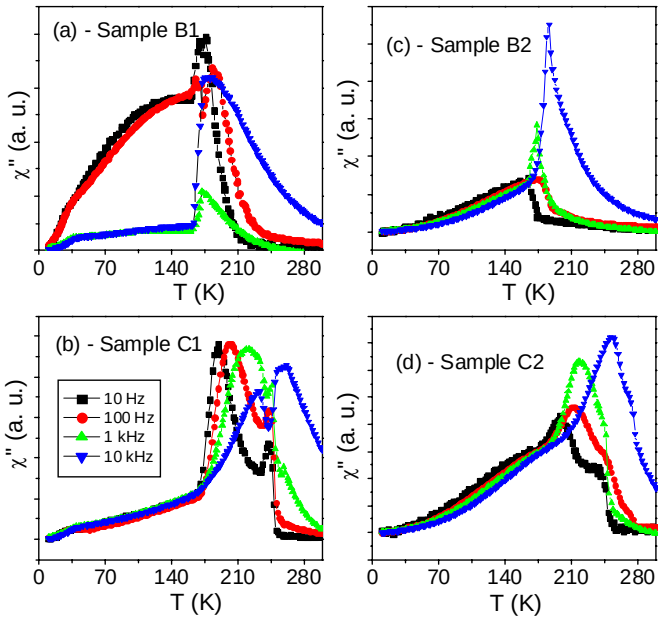

Fig. 4: Temperature dependence of imaginary part of susceptibility, χ", of (a) Sample B1, (b) Sample C1, (c) Sample B2 and (d) Sample C2 at 10 Hz – 10 kHz measuring frequency.

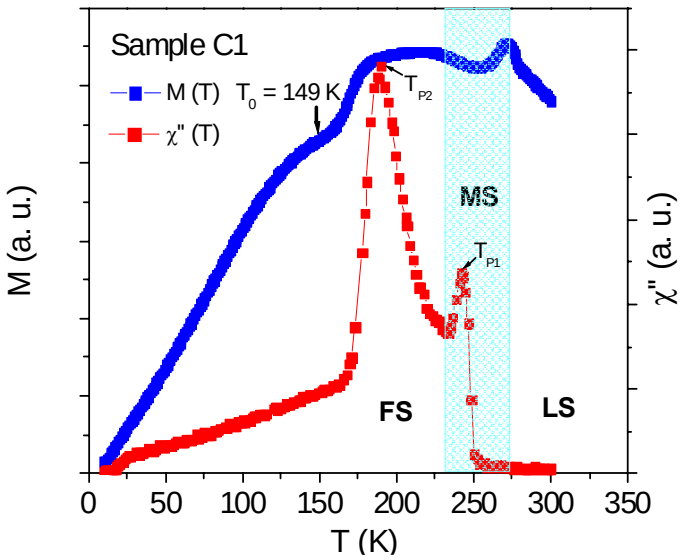

Fig. 5: Temperature dependences of ZFC magnetization and imaginary part of magnetic susceptibility, χ", of Sample C1 (Fe_3O_4 in dodecane). LS: Liquid Sate; MS: Mixed State; FS: Frozen State. T_o is the temperature at which the system enters a glassy state. T_{P1} and T_{P2} represent the magnetic behavior in the mixed and frozen states, respectively.

The ZFC and FC magnetization curves of all the samples investigated are shown in Figs 2 and 3. We label the samples as follows: Sample A1 (Fe_3O_4 in dry powder form), Sample B1 (Fe_3O_4 in hexane), Sample C1 (Fe_3O_4 in dodecane), Sample A2 ($CoFe_2O_4$ in dry powder form), Sample B2 ($CoFe_2O_4$ in hexane) and Sample C2 ($CoFe_2O_4$ in dodecane). For Samples A1 and A2, the relatively broad peak observed in the ZFC curves [Figs 2(a) and 3(a)] is consistent with the polydisperse nature of the magnetic nanoparticles with broad particle size distribution. However, the case is very different for the ferrofluids [Figs 2(b,c) and 3(b,c)]. The ZFC curves exhibit a sharp peak for Samples B1 and B2, while a small peak followed by the magnetic anomaly (i.e., the sharp drop in the ZFC magnetization at low temperature) are observed for Samples C1 and C2. The magnetic anomaly is only observed in ferrofluids having $T_B < T_F$ (i.e. for samples C1 and C2). In contrast, for the ferrofluids having $T_B > T_F$, the magnetic behavior in the liquid is not affected by the particle blocking.

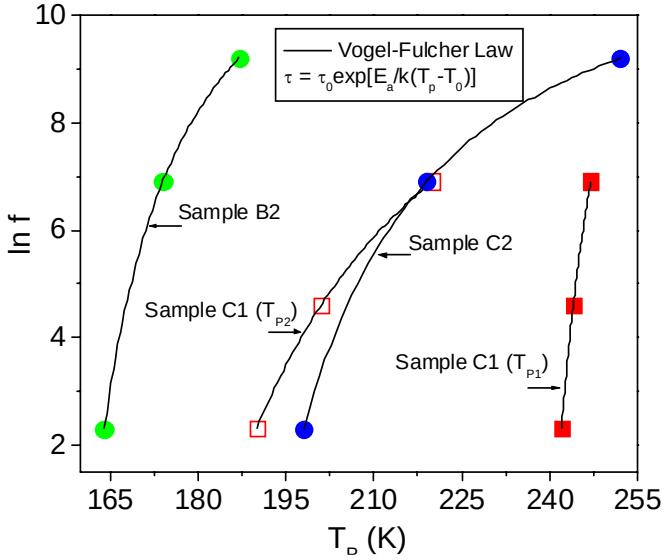

Fig. 6: The best fits of $T_p(f)$ data extracted from ac susceptibility measurements to the VF model for Sample C1 (for the cases of T_{p1} and T_{p2}), Sample B2 and Sample C2.

To correlate the physical origin of the two peaks in the AC complex susceptibility [8] to the peak and magnetic anomaly in the ZFC DC magnetization, we plot the real and imaginary susceptibility, χ' and χ'', respectively for different temperatures with increasing measuring frequency. In Fig. 4, the $\chi''(T)$ curves show a single peak for the ferrofluids having $T_B > T_F$ (Samples B1 and B2), while two distinct peaks are observed for the ferrofluids having $T_B < T_F$ (Samples C1 and C2). These are in excellent agreement with the features in the DC magnetization curves. Fig. 5 shows this correlation more

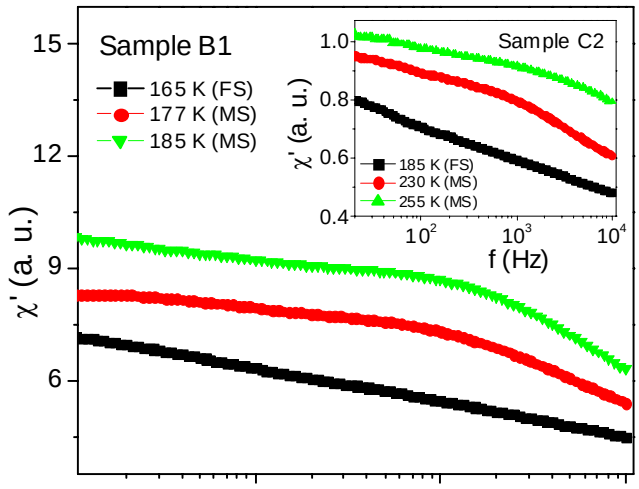

Fig. 7: Real part of magnetic susceptibility, χ', as a function of frequency of Sample B1 in the mixed state (at 177 K and 185 K) and in the frozen state (at 165 K). The inset shows the $\chi'(f)$ curves of Sample C2 in the mixed state (at 230 K and 255) and in the frozen state (at 185 K).

clearly, from which one can infer that the second peak in $\chi''(T)$ is ascribed to the blocking of magnetic nanoparticles, while the first peak in $\chi''(T)$ is associated with the freezing of the solvent. For our ferrofluids, the Vogel-Fulcher model has been found to fit the $\chi''(T)$ data well with acceptable fit parameters and the results are shown in Fig. 6. This also shows that our ferrofluids consist of interacting particles.

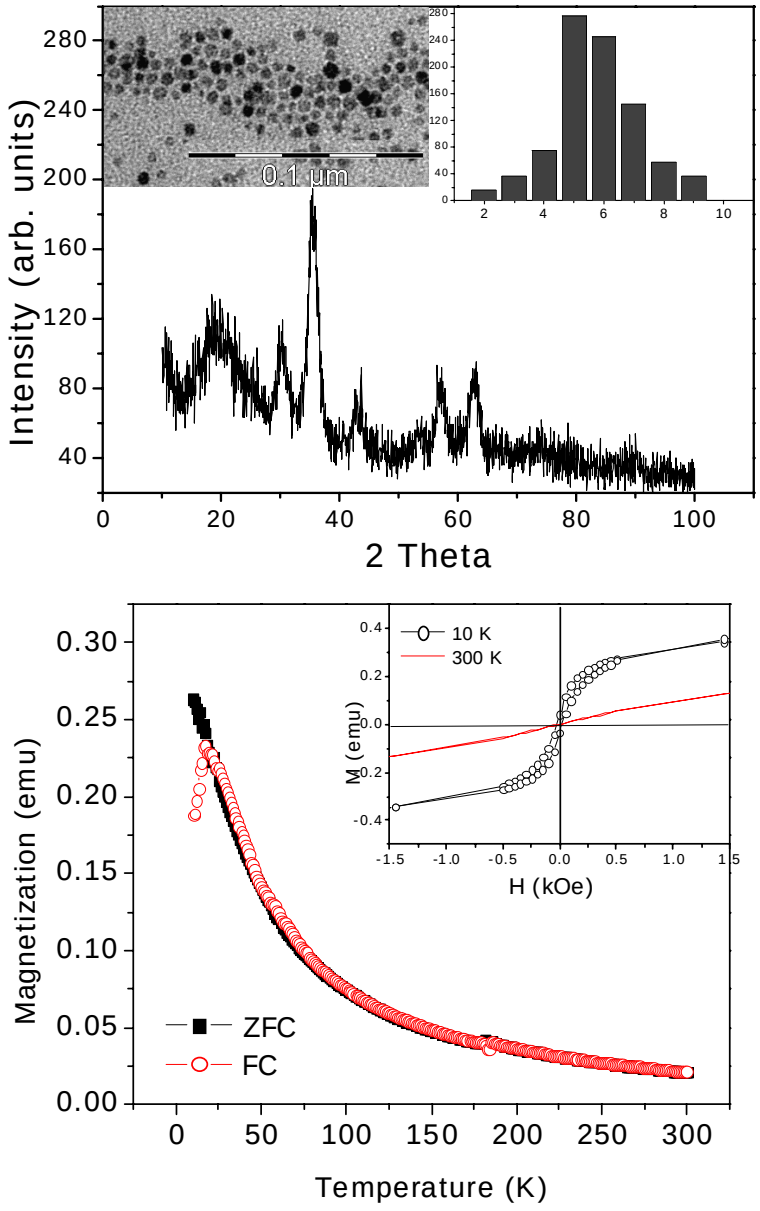

Fig. 8: Structural and magnetic characterization of ferrofluids with 6 nm Fe_3O_4 particles. Note the clear superparamagnetic response at high temperatures and sharp blocking characteristics at 18K.

Fig. 7 and its inset show the $\chi'(f)$ curves at three different temperatures for two representative ferrofluids (Sample B1 and Sample C2). We consistently note that for ferrofluids having $T_B > T_F$, a double slope feature in $\chi'(f)$ is observed in the mixed state which evidently indicates coexistence of both Brownian and Néel relaxation in this state, while $\chi'(f)$ shows only a linearly monotonic decrease in the frozen state, signifying the presence of Néel relaxation only [see Fig. 7]. For the ferrofluids having $T_B < T_F$ (the inset of Fig. 7), the non-monotonic, double slope feature in $\chi'(f)$ is observed at temperatures above T_B but in the frozen state, and $\chi'(f)$ only shows a linear feature as the temperature is lowered below T_B. This indicates the presence of Brownian relaxation in addition to Néel relaxation even in the frozen state. This trend seen in our samples is consistent with the recent observation that thermal motion of magnetic nanoparticles in ferrofluids continues well below the freezing temperature of the solvent or in the frozen state [5].

Based on these findings, we have realized that it is important to compare the properties of ferrofluids by varying the particle size. It is also important to improve the particle size distribution as well as reduce inter-particle interactions because the data shown in Figures 2 and 3 have a rather broad blocking temperature. Thus we extended our synthetic efforts to produce high quality, monodisperse

nanoparticles that have average sizes of 6nm, 8nm, 12nm and 16nm. This variety in size would provide further insights into the ferrofluid properties in addition to the variation in viscosity of the fluid medium that we discussed earlier. This required very careful variation of the synthesis parameters and the process has been somewhat time consuming. However, we have been successful in synthesizing 6 nm nanoparticles of Fe_3O_4 and obtain stable ferrofluid suspensions with these particles. The dispersion has been much improved. Figure 8 (top panel) shows the XRD and TEM images of the new batch of monodisperse 6 nm nanoparticles suspended in hexane. The bottom panel shows the zero-field cooled and field-cooled magnetization. The big difference in blocking characteristics is immediately visible. The blocking temperatue is now down to 18K and a very clean superparamagnetic response (1/T Curie type dependence) is observed from 25K all the way up to room temperature. A small feature around 180K is associated with the freezing transition of hexane. The inset of Fig. 8 (bottom panel) shows the M-H loops at 300K indicating no coercivity thus confirming superparamagnetic response whereas in the blocked state at 10K a coercivity of around 50*Oe* is observed.

The sensitivity of the magnetic properties of ferrofluids to the particle size, distribution and the carrier fluid properties is extremely important to elucidate when deciding on the optimal properties of the ferrofluids for targeted drug delivery, cell sorting, MRI contrast agent or hyperthermia applications. Thus our studies in the first year of the project have yielded critical fundamental information on the behavior of the magnetic properties of nanoparticles in the fluid, frozen and mixed (gel) states of the ferrofluid medium as the temperature and applied field are varied. We believe that the systematic information that we have been able to obtain from a comparative study of different types of ferrofluids has led us to narrow down on selection of the optimal characteristics. Our goal in the second year would be to continue studying the ferrofluid characteristics and also progress from organic solvents to water-based fluids. Colloidal stability of the water-based, biocompatible ferrofluids would be investigated for applications such as magnetic cell separation, drug delivery, hyperthermia and MRI contrast enhancement. A challenge in hyperthermia is to optimize ferrofluids for heating cells between 40 to 45 degrees Celcius to kill tumor cells at tolerable AC field frequency of around 120 kHz. Our synthesis and characterization efforts in the second year would be targeted towards achieving these conditions.

Project 2: Nanoporous/nano-wire structures and polymer nanotemplates for sensing and molecular manipulation

The first goal of this project is to use magnetic particles to apply mechanical stress to adherent cells and study the frequency-dependent cell growth. Many essential functions of mammalian cells, including movement, proliferation, and differentiation, can involve cellular recognition of and response to mechanical stimulation. Our first step was to validate the force application system and to investigate the effect of prolonged static or cyclic stress on cellular viscoelastic parameters and on the cell-substrate adhesion of human umbilical vein endothelial cells (HUVECs). With collagen-coated iron oxide beads (~5 μm in diameter) attached to the dorsal surfaces of HUVECs, we were able to apply constant stress to the cells by placing the culture dishes close to a permanent magnet (Figure 9). For cyclic force, the cell culture dish with the cells was placed on a stage that moved periodically left and right under the stationary magnet. Following static or cyclic stress application of a few hours duration, viscoelastic parameters of the cells were obtained from the measured time-dependent deformation produced by constant stress, analyzed using a suitable viscoelastic model [10], depicted in Figure 10.

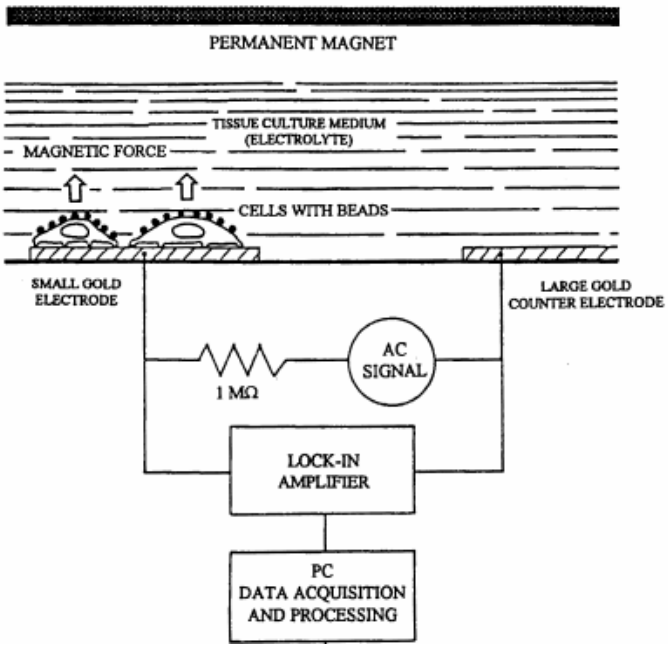

Fig. 10:Schematic for ECIS of HUVECs with attached collagen-coated iron oxide beads.

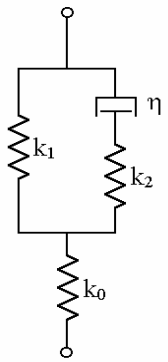

Fig. 10: Viscoelastic model for an adherent HUVECs, in which the springs represent elasticity and the dashpot represents viscosity. A spring (k_1) connected in parallel with a Maxwell body, which consists of a spring (k_2) and a dashpot (η) in series, is used to describe the viscoelasticity of the cell body, and another spring (k_0) in series with the cell body system is used to describe the elasticity of cell-substrate adhesion.

The time-dependent changes of cell morphology were measured by Electric Cell-substrate Impedance Sensing (ECIS). Our data (Table 1) show that applying 4 to 7 dyne/cm^2 of static stress to HUVECs for a few hours caused an increase of the elastic moduli and the viscosity of the cell body, and the elastic modulus of cell-substrate adhesion as well. On the other hand, cyclic stress of the same magnitude caused a decrease in all of these values. These observations indicate that the cellular viscoelastic properties and the cell-substrate adhesion of adherent epithelial cells can be altered by applied mechanical stress, either static or cyclic, but that the effects are strongly depend on the time course of stress application. Our next step will apply static or cyclic stress to HUVECs through iron oxide beads coated with different extracellular matrix proteins. We will examine whether the effect of static or cyclic stress is mediated by integrin-linked signaling or not. We will further study how cell growth depends on different time course of stress application.

Table 1 Summary of measured viscoelastic parameters of adherent HUVECs following a three hour application of static and cyclic mechanical stress via collagen-coated iron oxide beads. The values in this table are mean ± standard error of the mean for *n* independent measurements.

	k_0 (10 dyne/cm^2)	k_1 (10^3 dyne/cm^2)	k_2 (10^3 dyne/cm^2)	η (10^4 poise)
Control (n = 7)	4.1 ± 0.6	5.5 ± 0.7	6.6 ± 0.4	2.2 ± 0.3
Static (n = 10)	6.5 ± 0.8	7.2 ± 0.9	10.6 ± 1.5	3.1 ± 0.5
Cyclic (n = 12)	1.6 ± 0.3	2.3 ± 0.3	4.3 ± 0.3	1.6 ± 0.1

Project 3 - Carbon nanotube based sensors

The goal of this project is to develop multifunctional materials based on carbon nanotubes for electromagnetic sensing of biological and chemical analytes in the vapor and liquid phases. To our knowledge, embedding nanoparticles inside the cylindrical hollow core of carbon nanotubes and eventually using this nanocomposite peapod shaped structures for both electrical capacitive and magnetic inductive sensing of analytes has not been attempted in the past.

Carbon nanotubes are attractive candidates for supercapacitors due to their high electrical conductivity and controllable mesoporosity arising from the central nanotube canal and voids formed from nanotube entanglements. Hybrid nanocomposite materials composed of carbon nanotubes loaded with nanoparticles have also been studied for supercapacitors. We followed a variation of a procedure for synthesizing magnetic nanoparticles filled carbon nanotubes described in the literature [11]. The procedural steps are briefly described with schematic illustrations as shown below:

Synthesis procedure:

(a) Alumina membrane with carbon nanotubes produced by chemical vapor deposition (CVD) is (b) brought in contact with ferrofluid (Fe_3O_4, $Au@Fe_3O_4$ solution in hexane) (c) Ferrofluid invades pores. (d) Carrier fluid is dried to leave only magnetic particles in CNTs. (e) Alumina membrane is dissolved in NaOH to produce magnetic CNTs.

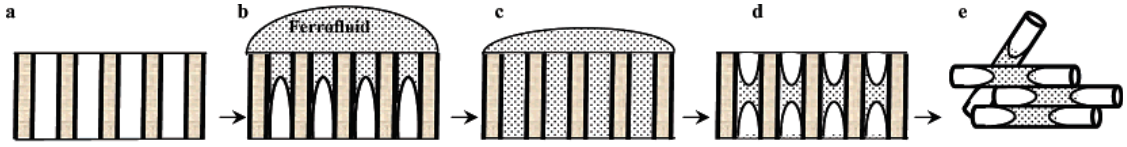

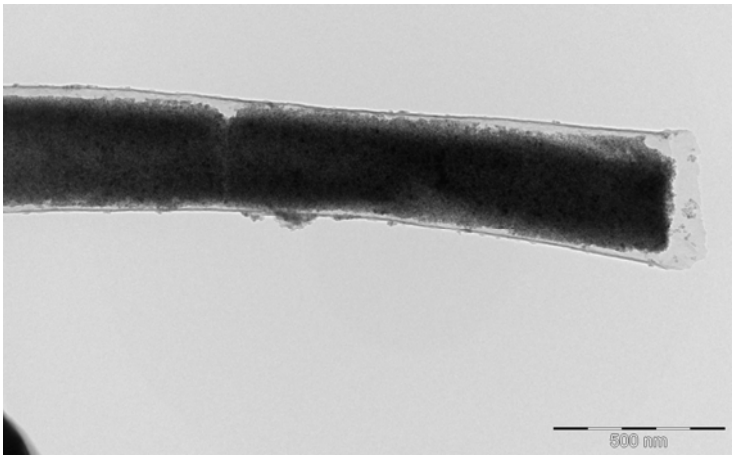

Fig. 11: (top) Schematic of the multi-step synthesis procedure for producing carbon nanotubes loaded with magnetic nanoparticles. (Bottom) TEM image of a filled nanotube

We have synthesized 300-400 nm diameter CNTs using alumina template with pore size 200 nm filled with 6nm Fe_3O_4 nanoparticles (Fig.11). Note the uniform dispersion of the nanoparticles throughout the nanotube. **This is a significant breakthrough in our attempts to achieve dual functionality of these filled magnetic nanotubes –viz. capacitive sensing due to the dielectric response of the CNT and magnetic property rendered by the nanoparticles inside the tubes.** We are currently in the process of measuring the physical properties of these magnetic nanotubes. In the second year, we expect to progress towards using an assembly of these nanotubes and setting up experiments to monitor their properties for impedance sensing using both electric and magnetic fields.

Our initial goal was to make CNTs with different diameters (down to 50nm). For that we purchased commercial alumina templates with advertised pore size of 20 nm. However, our repeated attempts to synthesize CNTs over the past few months with smaller diameter by changing the reaction conditions such as temperature, flow rates of gases, reaction time etc. were in vain. We were consistently getting 250 – 300 nm diameter CNTs all the time. A TEM analysis of the commercial templates of 20 nm and 200nm pore size (annealed at 740^0C) (see Fig. 12 below) showed that the actual pore sizes are 250 – 300 nm. Similar results were also reported by other groups in the literature [12,13] so this appears to be a common problem associated with the quality of commercial alumina templates subject to annealing. We intend to continue to the next stage with the successful batch of larger diameter CNTs loaded with magnetic nanoparticles.

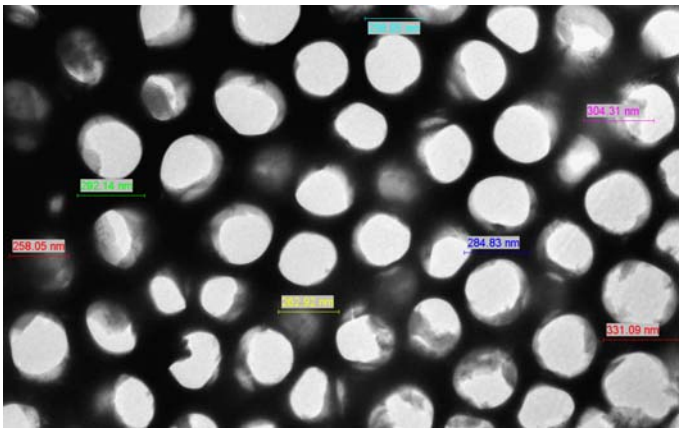

Fig. 12: TEM image of commercially purchased alumina templates after annealing

Project 4 – Functional materials for affecting cell proliferation and locomotion

In this project, we are looking at several nanoscale structures where the basic functionality such as magnetic and metallic properties can be used for biomedical diagnostics and cell manipulation. Dr. Susmita Pal has been active in this area and has synthesized several batches of core-shell nanoparticles with Au shell and Fe_3O_4 core structure. These have been well characterized and are the subject of two papers communicated for publication. A brief progress report of this project is given below.

The core-shell type magnetic nanoparticles are receiving considerable attention because this heterostructure offers opportunities to develop devices and materials with new functions for magnetic recording, sensing and bio-medical applications [14–22]. Superparamagnetic nanoparticles with suitable biocompatible coatings are becoming important in the fields of biotechnology and medicine. Applications include magnetic resonance imaging, magnetic separation, tissue engineering, drug delivery/targeting [15-22] and so on. For these applications, the magnetic nanoparticles are required to possess uniform particle shape, narrow size distribution, good corrosion resistance and high magnetic moment [17-18]. To date superparamagnetic iron-based oxide (magnetite and maghemite) nanoparticles are being widely used in these areas [15, 22-27]. Recently, incorporation of optically active components onto magnetic nanoparticles has opened a new direction of research. Using gold (Au) coating, the magnetic nanoparticles, especially high moment magnetic nanoparticles, can be stabilized more efficiently and readily functionalized through the well developed Au-S chemistry in thiol capped gold nanoparticle [28,29]. The coating also renders the magnetic nanoparticles with plasmonic properties. This makes the core/shell composite nanoparticles extremely interesting for magnetic, optical, and biomedical applications. Here we present a procedure for the synthesis of Au-coated Fe_3O_4 nanoparticles with controlled particle size.

Experimental:

The preparation of gold coated Fe_3O_4 nanoparticles involved an initial synthesis of Fe_3O_4 nanoparticles as seeds and a subsequent reduction of gold acetate [$Au(OOCCH_3)_3$] in the presence of the seeds.

Synthesis of 6 nm Fe_3O_4 nanoparticles: The oleylamine and oleic acid capped 6 nm Fe_3O_4 nanoparticles were synthesized using a standard procedure.[35] In a typical synthesis process, 10 mmol 1,2- hexadecanediol, 6 mmol oleic cid, 6 mmol oleylamine and 20 ml benzyl ether were added to 2 mmol Iron (III) acetylacetonate. The mixture was stirred magnetically under a flow of argon. The mixture was heated to 200 ^{0}C for 2 h and then refluxed at ~300^{0}C for another 1 hr in presence of argon. The reaction mixture was cooled to room temperature by removing the heat source. 40 ml ethanol was added to the mixture and a black precipitate was separated by centrifugation. The black product was dissolved in hexane in presence of oleic acid (~0.05 ml) and oleylamine (~0.05 ml) and centrifuged to remove the undispersed residue. The product of 6 nm Fe_3O_4 particle was then precipitated with ethanol, centrifuged to remove the solvent and redispersed into hexane.

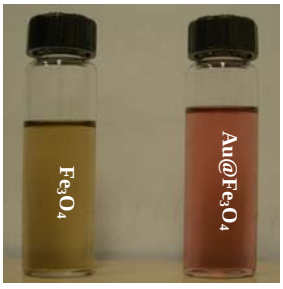

Fig. 13: Fe_3O_4 and gold coated Fe_3O_4 solution in hexane.

Gold-coated Fe_3O_4 nanoparticle: After 1 hr refluxing of Fe_3O_4 nanoparticles as described above, the reaction solution was directly used without purification. In a typical synthesis, 10 mL of the benzyl ether reaction solution of Fe_3O_4 nanoparticles (~ 0.33 mmol Fe_3O_4), 0.83 g (2.2 mmol) $Au(OOCCH_3)_3$, 3.1 g (12 mmol) 1.2-hexadecanediol, 0.5 mL (~1.5 mmol) oleic acid, 3 mL (~ 9 mmol) oleylamine were added into 30 mL benzyl ether. Under argon atmosphere, the reaction solution was heated to 180–190 ^{0}C at 10 ^{0}C min^{-1} with vigorous stirring and was kept at this temperature for 1.5 h. After cooling down to room temperature, ethanol was added into the solution. A dark-purple material was precipitated and separated by centrifuging. The precipitated product was washed with ethanol, and re-dispersed in hexane in the presence of ~ 75mM each of oleic acid and oleylamine. The nanoparticle solution appeared dark purple (Fig.13).

Characterization:

Transmission electron microscopy (TEM): TEM was performed using Morgagni 268D (100 kV) Electron Microscope. The nanoparticle samples dispersed in hexane solution were cast onto a carbon-coated copper grid followed by evaporation at room temperature. Fig.14 shows a

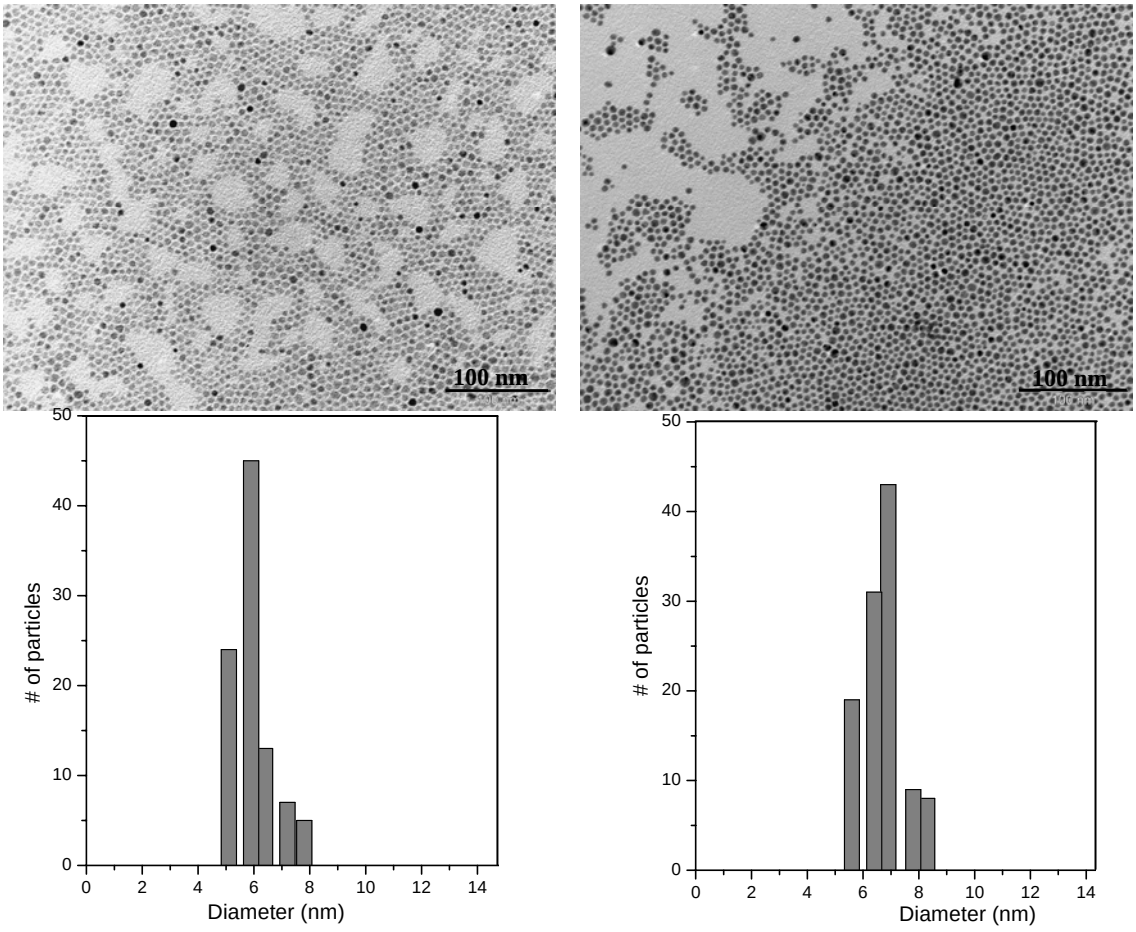

Fig. 14: TEM images (top) and size distributions (bottom) of Fe_3O_4 nanoparticles (a) before and (b) after coating with Au shell.

representative set of TEM micrographs of Fe_3O_4 nanoparticles before and after the formation of a gold shell. The well isolated particles show non-spherical shape in Fe_3O_4, whereas nearly spherical shape is observed in gold coated Fe_3O_4. The two major findings from the morphological comparison are: (i) the particles after coating with Au appear much darker than before coating of Fe_3O_4 nanoparticles, (ii) the average particle sizes changed from 5.9 ± 0.5 nm for particles before coatings (Fig.14a) to 6.9 ± 0.5 nm for the particles after coating (Fig.14b) with Au. We plan to do HRTEM on this core shell sample to get more information about the thickness of the gold shell.

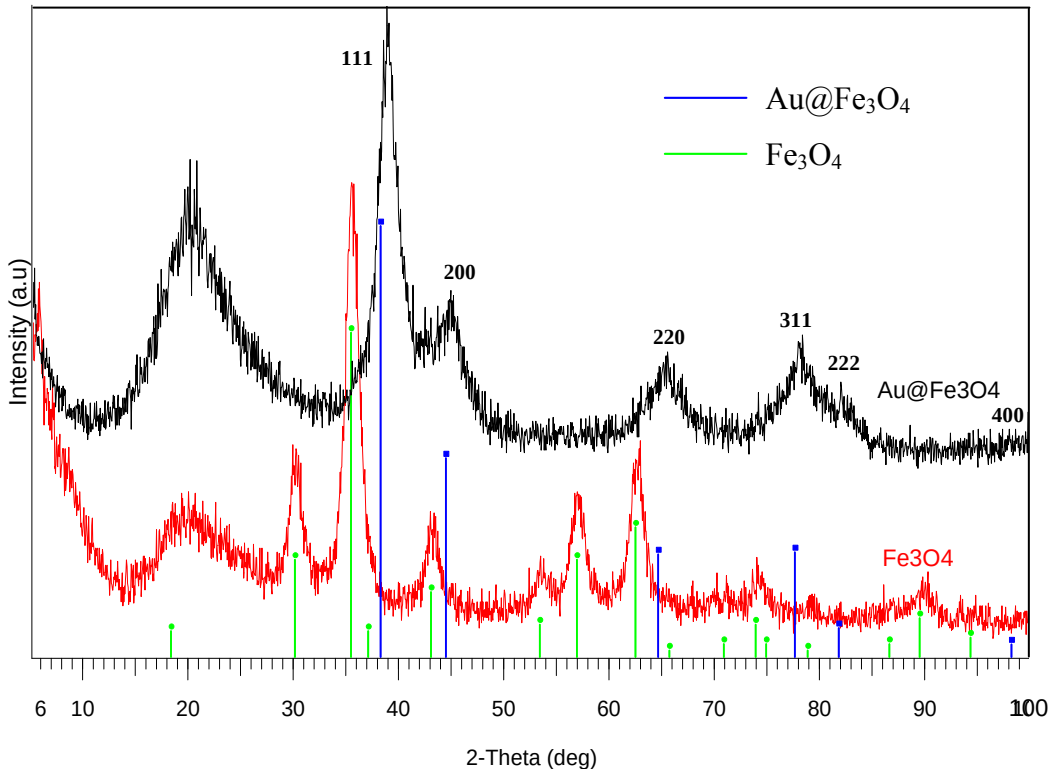

Fig. 15: XRD data of Fe_3O_4 and gold coated Fe_3O_4 nanoparticles.

XRD analysis:

The samples were characterized by Bruker D8 Focus X-ray diffractometer. The data were collected from $2\theta = 5^0$ to 100^0 using CuK_α source. The XRD data (Fig. 15) of $Au@Fe_3O_4$ nanoparticles shows the diffraction peaks corresponding to the gold in cubic phase. The diffraction peaks correspond to Fe_3O_4 nanoparticles are absent in gold coated Fe_3O_4 nanoparticles which is a strong evidence for complete coverage of the iron oxide core by gold.

Magnetic characterization:

We have studied the magnetic properties including temperature dependent zero-field cooled (ZFC) and field cooled (FC) magnetization (M-T), M vs H, AC and radio-frequency (RF) transverse susceptibility using a Physical Properties Measurement System (PPMS) from Quantum Design available in our Functional Materials Laboratory. The M versus T data

measured at H = 200 Oe in ZFC-FC modes for the Fe_3O_4 and Fe_3O_4@Au nanoparticles show superparamagnetic response at high T with blocking temperature (T_B) around 35 K and 40 K, respectively (Fig.16). The slight increase in blocking temperature for Au-coated particles could be due to the overall increase in particle size as observed from TEM.

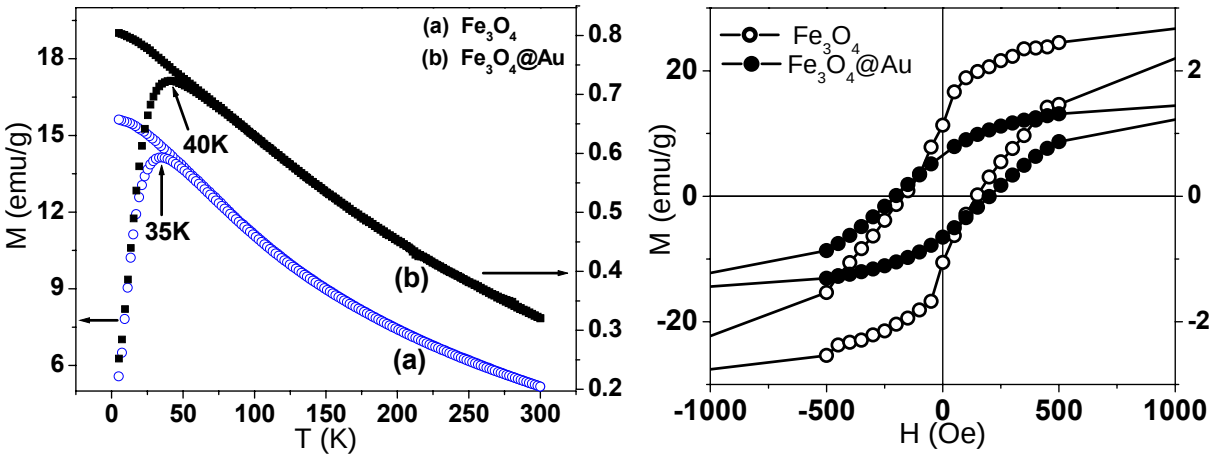

Fig. 16: (Left) Zero-field cooled and field-cooled magnetization data for (a) bare Fe_3O_4 and (b)core-shell Fe_3O_4@Au nanoparticles. (Right) The M-H hysteresis loops taken at 5K after field cooling.

M versus H (also shown in Fig. 16) was measured at applied fields of ± 50 kOe at 5K under ZFC-FC modes. The saturation magnetization (M_s) values of Fe_3O_4 NPs and Fe_3O_4@Au are 33 emu/g and 1.8 emu/g respectively which are significantly lower than that of bulk Fe_3O_4 (M_s = 84

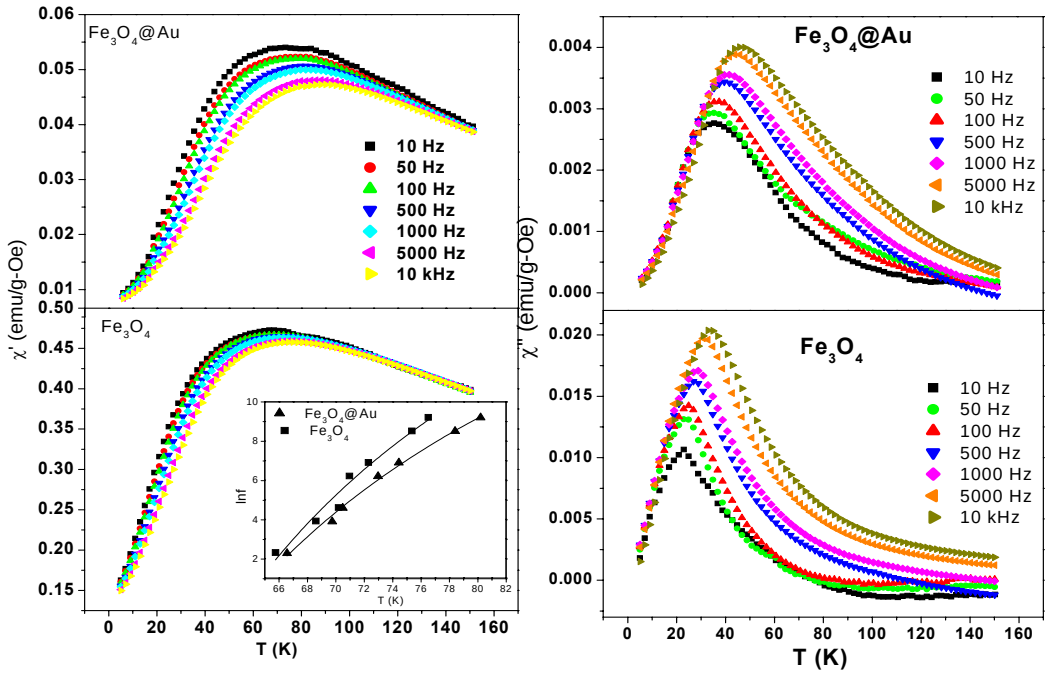

Fig. 17: Real (χ') and imaginary (χ") parts of the AC susceptibility in Fe_3O_4@Au nanoparticles at different AC frequencies

emu/g). This reduction is expected in nanoparticles as the surface magnetic order can be affected by structural distortions that cause spin canting [36]. We measured the M-H loops after field cooling to 5K to look for any possible exchange bias that could result in coercivity enhancement. However, the loops were symmetric and no exchange bias was found for both particle systems.

The temperature dependent (5K – 150 K) AC susceptibility (both in phase χ' (T) and out of phase χ''(T)) were measured over the frequency window from 10 Hz to 10 kHz for both uncoated and Au coated samples (Fig. 17). The magnetic relaxation of non-interacting nanoparticles is expected to follow the thermally activated Néel-Arrhenius law given by the expression $f = f_0 \exp(-E_a/k_B T_B)$ where f_0 (attempt frequency) is of the order of $10^9 - 10^{13}$ Hz, k_B is Boltzmann constant and E_a is the anisotropy energy. In the case of weakly interacting nanoparticles, the system is expected to conform to the framework of the Vogel-Fulcher relaxation: $f = f_0 \exp(-E_a/k_B(T_B - T_0))$ with T_0 being the effective strength of interparticle interactions. As expected from these expressions, the blocking temperature increases with increasing frequency (Fig.17). It is clearly seen that the T_B shifts to a slightly higher value in Fe_3O_4@Au compared to the uncoated Fe_3O_4 NPs which also supports the DC magnetization (M vs. T) results. Fits to the Néel-Arrhenius model yields unphysical values for f_0 (10^{20} Hz) whereas reasonable values for f_0 are obtained from fits to the Vogel-Fulcher relation. The fit values of f_0, E_a/k_B and T_0 for the uncoated (coated) particles are 5.0 $\times 10^{13}$ (5.0×10^{12}) Hz, 1003 (1042)K and 32 (28)K, respectively, and the plots are shown in the inset figure. These parameters extracted from the fits suggest that the interparticle interaction is reduced a bit in gold coated nanoparticles.

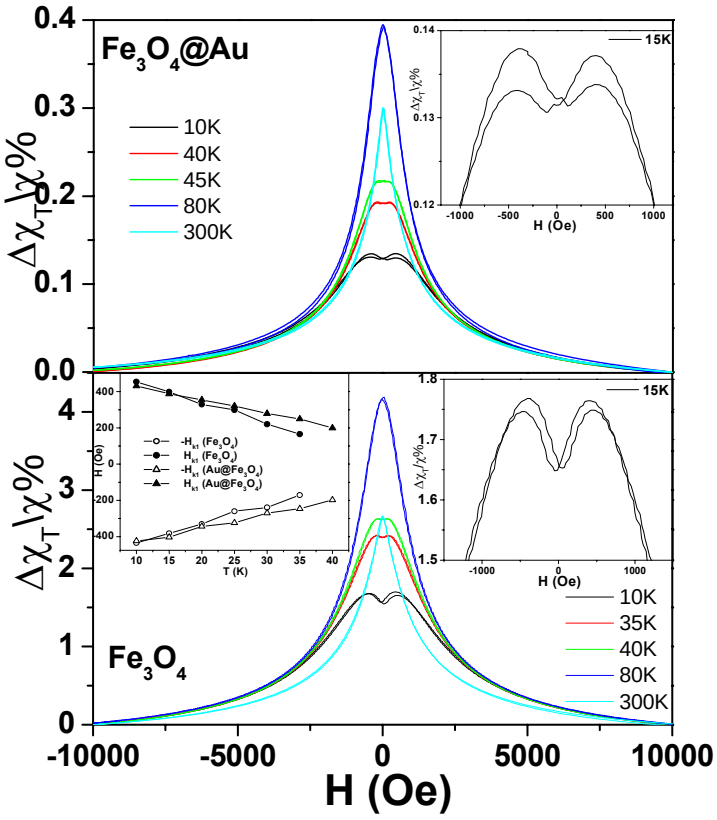

Fig. 18: RF transverse susceptibility of magnetic nanoparticles showing the variation of magnetic anisotropy fields.

We have also measured the field-dependent transverse susceptibility (TS) data for field scans of ± 10 kOe over a temperature range 10 K < T < 300 K for both the uncoated and Au-coated nanoparticle systems (Fig. 18). The two peaks corresponding to the anisotropy field ($\pm H_k$) were observed below blocking temperature and the peaks merge into a single peak at H = 0 above blocking temperature consistent with earlier studies on nanoparticle samples.[3, 4] At T = 10K, the anisotropy field is around 450 Oe which is in range of values (250 to 500 Oe) typically observed in Fe_3O_4 nanoparticles.

Detailed magnetic characterization of the magnetic nanoparticles presented above confirm that these particles are of high quality and exhibit the desirable AC relaxation response suitable for applications in biomedicine. In the next year, we anticipate functionalization of these nanoparticles with biological coatings. Optical activity will also be studied. The functionalized nanoparticles will also be injected into cells and Electrochemical Impedance Sensing (ECIS) will be used to monitor cell motility and response to external field stimuli.

Task II: Multifunctional composites for communication and energy applications

This task is divided into the following projects –

Project 5 – Tunable multifunctional nano- and heterostructures for RF and microwave applications

Project 6 – Flexible photonic materials for solar-based energy sources

During this quarter, work was continued on both Projects 5 and 6. These activities and results are outlined in the following:

Project 5 - Tunable multifunctional nano- and heterostructures for RF and microwave applications

Integration of ferromagnetic thin films with ferroelectric thin films to enable manipulation of magnetic properties via electrical means holds intriguing possibilities for novel magneto-electronic devices. These multifunctional structures offer possible applications in several technologies, including memory devices that allow electrical encoding and magnetic readout, voltage gain devices, ultra sensitive magnetic field sensors that operate at room temperature, and microwave frequency transducers [37].

This project is aimed at fabricating artificial multiferroic structures by bringing a ferroelectric and a ferroelectric material together to form interfaces that will enable the coupling of the magnetization and electric polarization via interfacial strain. We are investigating two possible thin film nanostructures that are fabricated by a laser ablation technique. These structures are: (1) multilayers of ferromagnetic and ferroelectric materials with thicknesses in the range of 50-200 nm, (2) embedded nanopillars of the ferromagnetic material within a thin film of the ferroelectric material. As the manifestation of the coupling between the order parameters in these structures is due to the interfacial strain at the interfaces of the magnetic and ferroelectric layers, epitaxial growth of the layers is essential to maximize the transfer of stress from one material system to the other. Both these structures are designed to leverage the enhanced surface area to maximize the strain-mediated coupling between the magnetic and electric order parameters. The material systems of interest are $BiFeO_3/CoFe_2O_4$, $BaTiO_3/CoFe_2O_4$ [38] and $PZT/CoFe_2O_4$ [39].

The first group of materials to be investigated is $CoFe_2O_4$ and PZT. Since the magneto-electric coupling between the two materials due to interfacial strain is being investigated, the increased surface area is expected to enhance this effect. Our aim is to manipulate the growth conditions to fabricate structures that contain nano-pillars of $CoFe_2O_4$ surrounded by PZT. This is achieved by depositing material on the substrate at an oblique angle. The formation of a crystalline phase on a substrate is determined by the activation energy. Films tend to grow preferentially in low energy

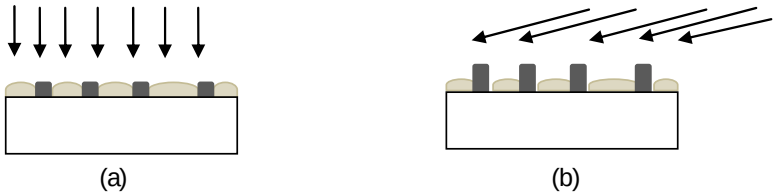

Fig. 19: Polycrystalline film growth with a preferred direction of growth in (a) normal incident deposition, (b) oblique incident deposition.

directions. In an oblique incident growth process the initial islands that grow preferentially in a specific crystal orientation show a high rate of growth in the vertical direction while suppressing growth in the other direction due to strong shadowing. This effect is shown in Fig. 19.

Films of $CoFe_2O_4$ were deposited on silicon substrates by ablating a $CoFe_2O_4$ target at a growth temperature of 450°C with normal incidence and with an oblique angle of incidence (60°). X-ray diffraction patterns of the films deposited under the two conditions are shown in Fig. 20. The oblique-angle deposition has enhanced the crystal structure formation in the (111) direction.

The next phase of this project involved the deposition of PZT films on the $CoFe_2O_4$ nano-structures and investigation of magnetic and electric properties of these bilayer and multilayered structures.

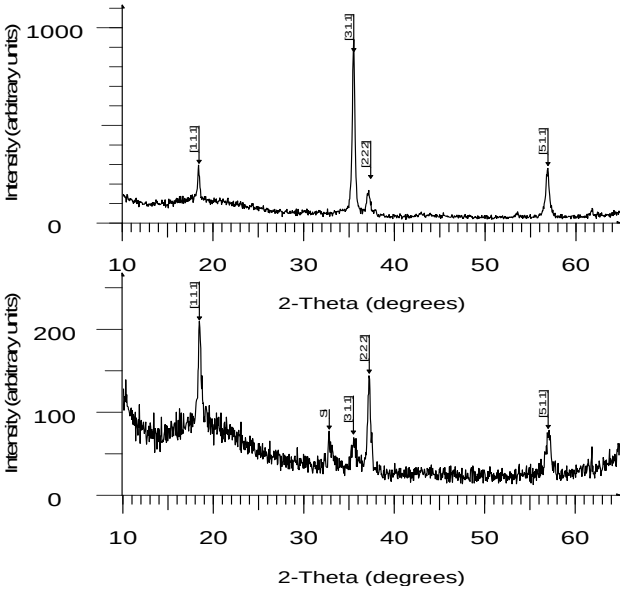

Fig. 20: $CoFe_2O_4$ films deposited on silicon with (above) normal incidence, (below) at an incident angle of 60°.

Polycrystalline CFO/PZT structures: Direct deposition of PZT on silicon substrates is not possible as a result of silicon diffusion that disrupts nucleation of PZT [40]. Growth of PZT on silicon with platinum buffer layers has been reported [40]. We have used preferentially oriented

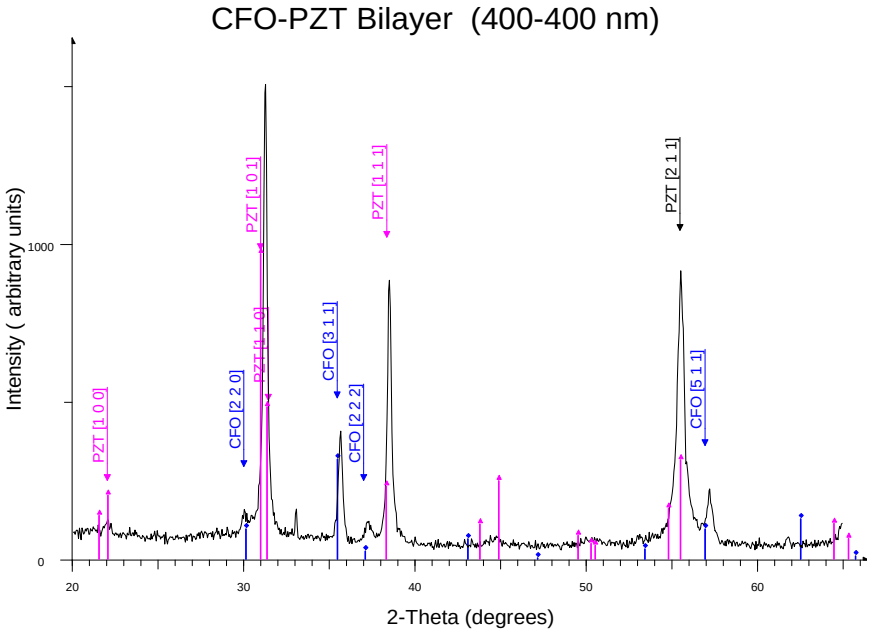

Fig. 21: X-ray diffraction θ-2θ scan of a CFO/PZT film deposited on a silicon substrate.

polycrystalline films of CFO as buffer layers to grow PZT on silicon. X-ray diffraction pattern from a CFO/PZT bilayer on silicon is presented in Fig. 21. For this structure, in which the thickness of the CFO layer is about 400 nm, most of the high-intensity peaks corresponding to powder patterns of CFO and PZT are present indicating that the films contain grains with random orientations. The AFM image of the top PZT surface (Fig. 22) also indicates randomly oriented grains of varying dimensions.

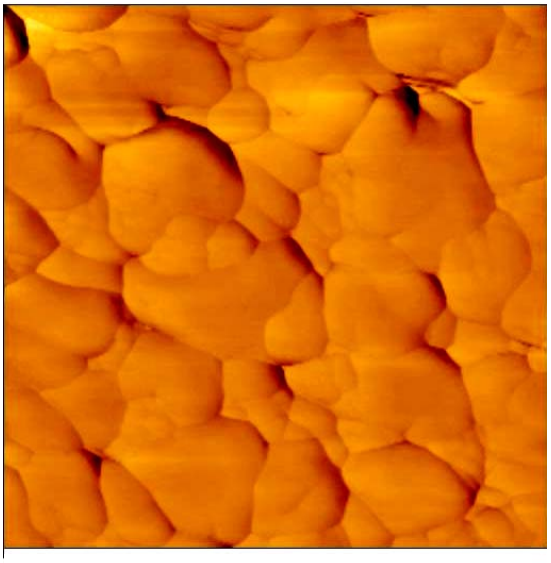

Fig. 22: AFM image of the PZT film surface of a CFO/PZT film deposited on silicon.

For a relatively thin (<200 nm) CFO layer on silicon where it grows preferentially in the (111) direction, the PZT layer deposited on CFO appeared polycrystalline. However, an enhancement in the (111) direction was observed in the PZT films. A cross-sectional view of these bilayers observed by Focused Ion Beam (FIB) etching and imaging showed the clear interface between the two layers and columnar growth that is indicative of preferentially oriented films (Figs. 23 (a) & (b)).

Room-temperature magnetic hysteresis of the bilayer films have been measured using the Physical Property Measurement System (PPMS). Fig. 24 shows the behavior of magnetization for a CFO film and that for a CFO/PZT bilayer with similar CFO film thicknesses. Clearly, the presence of the non-magnetic PZT layer has significantly reduced the remanent field and the coercivity. This indicates possible coupling between the magnetic and the electric order parameters. However, this preliminary result is non-conclusive and further measurements including electrical polarization in magnetic fields have to be made to confirm this effect.

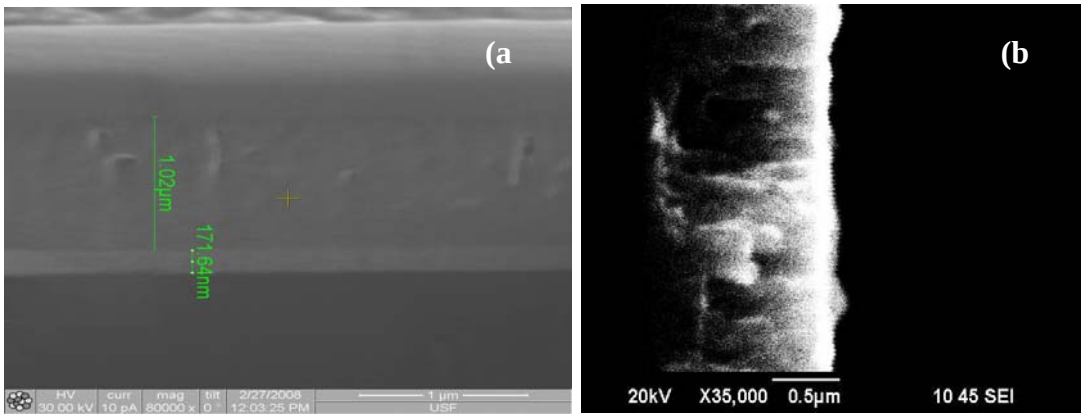

Fig. 23: Cross-section view of a CFO/PZT film on a silicon substrate, where (a) shows the interface between the films and (b) shows the columnar growth.

Epitaxial growth of CFO/PZT bilayers: Epitaxial growth of PZT films on single crystal MgO substrates has already been demonstrated [41]. However, prior to this work epitaxial growth of CFO/PZT layers has not been reported. Table 2 compares the structure and lattice parameters of

CFO, PZT and the substrates that are used in our experiments. The base of the CFO unit cell can accommodate 4 unit cells of MgO with a lattice mismatch that is less than 1%. Therefore, epitaxial growth of CFO on Mg is viable. Similarly, the lattice mismatch between CFO and PZT is about 4%. In this work, we have developed the growth conditions to deposit CFO films on MgO substrates epitaxially, followed by epitaxial growth of PZT on CFO. We have used x-ray diffraction techniques to confirm the epitaxial nature of the bilayers.

Table 2

Material	**Structure**	**Lattice Constant A° (a)**	**Lattice Constant A° (c)**
$CoFe_2O_4$	F.C.C	8.391	
PZT	Tetragonal	4.035	4.131
MgO	Cubic	4.216	
Sapphire	Hexagonal	4.765	12.991
YSZ	Cubic	5.41	

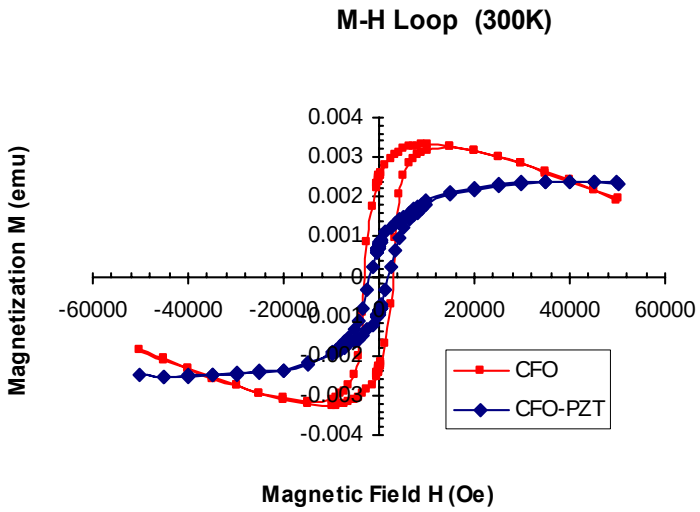

Fig. 24: Ferromagnetic hysteresis loop for a CFO film on silicon and a CFO/PZT bilayer on silicon.

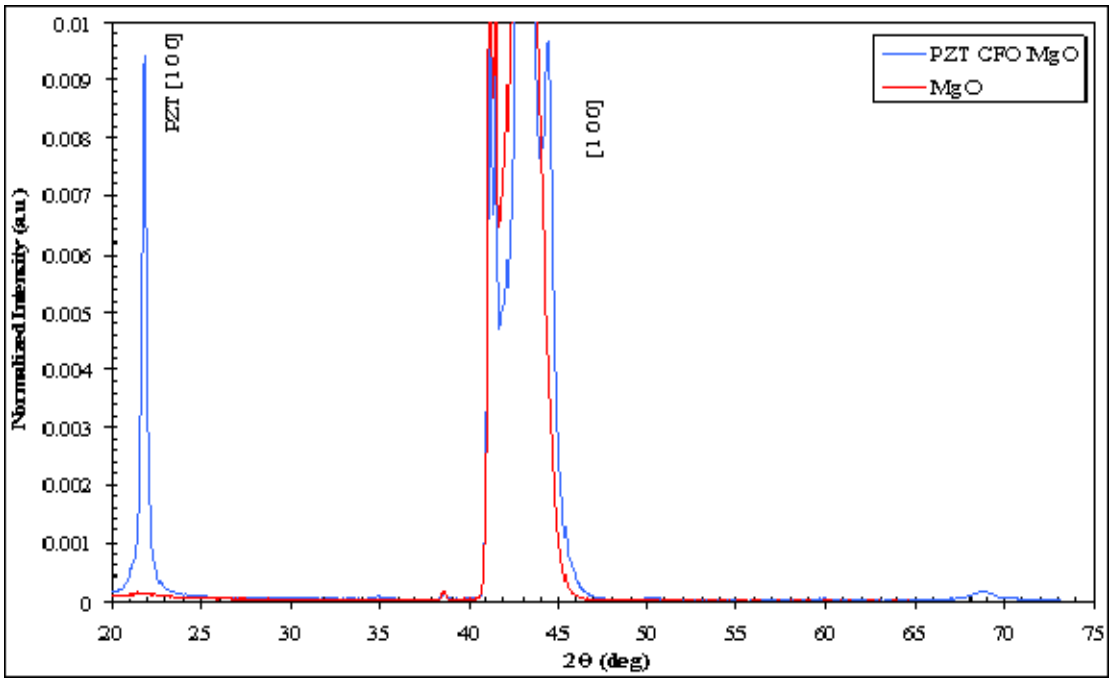

Fig. 25: X-ray diffraction (θ-2θ scan) of a CFO/PZT film deposited on a single crystal MgO (100) substrate.

Fig. 25 shows an x-ray diffraction pattern of a CFO/PZT bilayer on a (100) MgO substrate. A θ-2θ scan of the bilayer shows only the (100) orientations of PZT and a set of overlapped peaks corresponding to (200) orientation of PZT, MgO and (100) CFO.

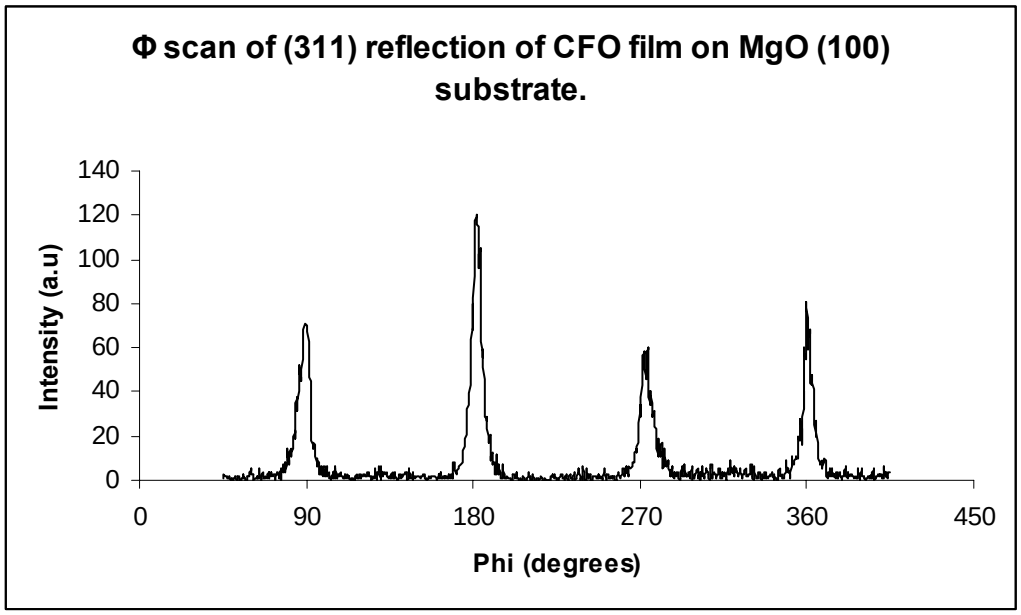

Fig. 26: X-ray diffraction ϕ scan of an epitaxial CFO film on a MgO (100) substrate around the (311) plane.

Epitaxial nature of a CFO film on MgO and a CFO/PZT bilayer were confirmed by ϕ scans around a specific lattice plane. Fig. 26 is a scan of a CFO film on MgO around the (311) lattice plane of CFO. Diffraction from this plane is absent in MgO. Repetition of the diffraction peaks every 90 degrees corresponds to the 4-fold symmetry of the CFO cubic structure. This confirms epitaxial growth of CFO on MgO substrates.

Fig. 27 is a ϕ scan of a CFO/PZT bilayer on MgO around the (101) plane of PZT. This result confirms the epitaxial nature of the PZT film. Transmission electron microscopy (TEM) imaging of the films to support these results is underway. We will also be investigating the ferromagnetic hysteresis of these films. Fig. 18 is an AFM scan of the CFO/PZT bilayer top surface. Well-arranged domains are indicative of epitaxial growth.

In summary, in this project, we have developed growth conditions for fabricating CFO/PZT bilayers. Preliminary ferromagnetic hysteresis data suggest possible coupling between magnetic and electric order parameters of the ferromagnetic and ferroelectric layers. Bilayer structures of CFO/PZT have also been grown epitaxially. We will explore the advantages offered by epitaxial films over preferentially oriented films in multiferroic coupling.

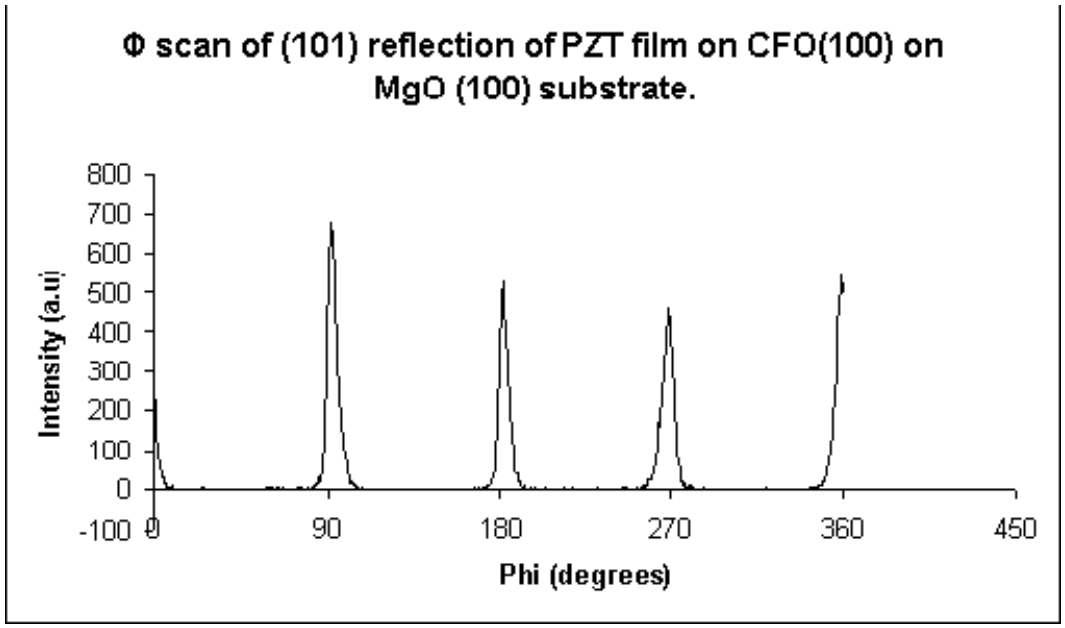

Fig. 27: X-ray diffraction ϕ scan of an epitaxial CFO/PZT film on a MgO (100) substrate around the (101) plane.

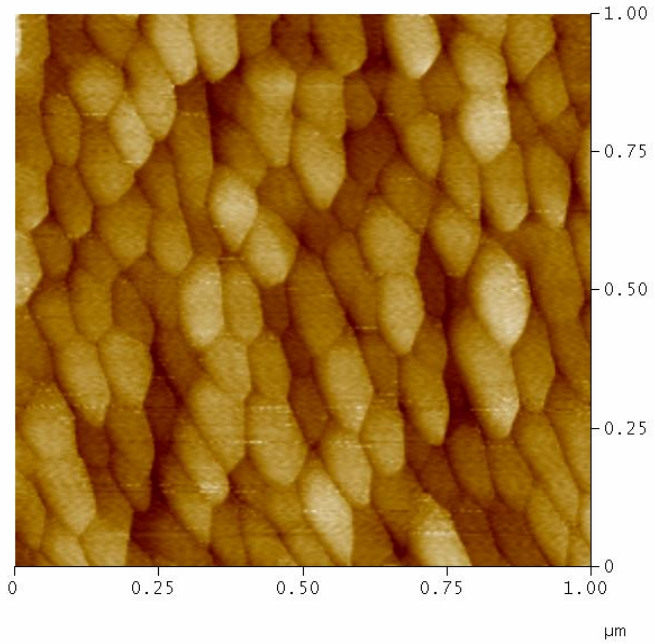

Fig. 28: AFM scan of the PZT film surface in CFO/PZT epitaxial films.

Project 6 - Flexible photonic materials for solar-based energy sources

Quantum dots (QD) of PbSe and PbS have been shown to produce multiple excitons with the absorption of a single uv photon [42]. Efficient dissociation of these excitions will produce a high density of charge carriers. A solar cell based on QDs has the potential to produce very large currents leading to conversion efficiencies well above the thermodynamic limit. In this project we are investigating the possibility of producing efficient solar devices that are flexible and cost-effective by combining QDs with semiconducting polymers.

The quantized energy states in a quantum dot (QD) the e-h pairs are formed in bound states (excitons). The binding energy between the electron and the hole is 0.1-1 eV [43]. The separation between the 1st ($1S_e$) and the 2nd ($1P_e$) electron quantum levels can be 300-500 meV, which is about 10 times larger than the longitudinal optical phonon energy (~40 meV) [43]. The electron's ability to relax via phonon emission is suppressed creating a *"phonon bottleneck"*. Instead, excess energy (at least $1E_g$) is coupled into an electron in the valance band to generate another e-h pair via an Auger-type impact ionization process [44]. A solar cell based on QDs has the potential to produce very large currents leading to conversion efficiencies well above the thermodynamic limit. Quantum yield, which is the number of ground-state excitons generated per photon, in excess of 300% has been reported for quantum dots of PbSe [45].

The interlevel spacing in conduction or valance band for a quantum dot of diameter d is given by $\frac{h^2}{8m^* d^2}\left(n_x^2 + n_y^2 + n_z^2\right)$, where m^* is the corresponding effective mass. Larger quantum level spacings correspond to longer lifetime of the excitons. Relatively small electron and hole effective masses of PbSe and PbS facilitate multiple exciton generation in QDs of these materials. For PbSe: E_g = 0.26 eV, m_e^*=0.07, and m_h^*=0.06, while for PbS: E_g = 0.37 eV, m_e^*=0.1, and m_h^*=0.1. A PbSe QD having a diameter of 7 nm will therefore have a band gap of 0.48 eV. While size tunability of QDs enables manipulation of the band gap, alloying of PbS and PbSe also provides an alternate way to change the band gap and quantum levels without having to decrease the QD size significantly. Larger QD sizes correspond to higher photon absorption cross-sections. Subsequent to developing a thorough understanding of the basic physics and functionality of QDs, a hybrid cell structure consisting of PbSe QDs, nanoparticles

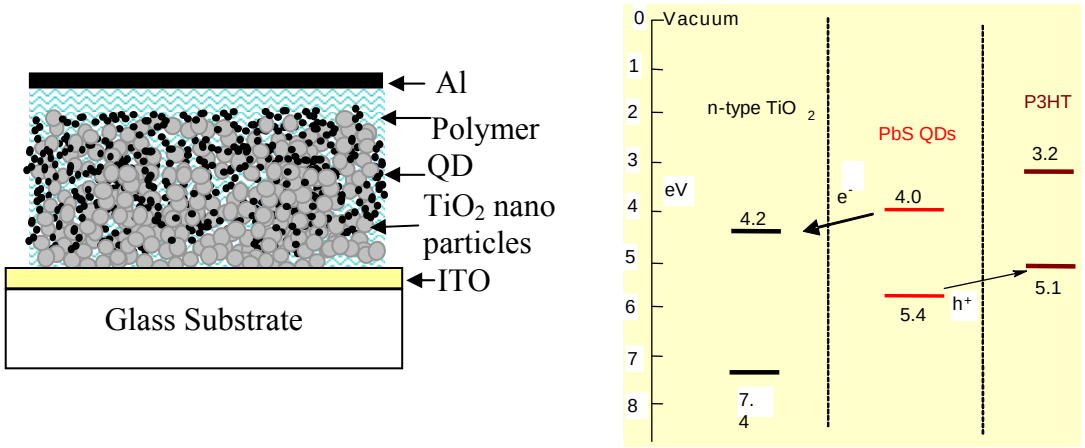

Fig. 29: Proposed hybrid structure with nanoporous TiO_2/QD/P3HT and energy band alignment of the three components

of TiO_2 and a p-type polymer will be constructed. The proposed structure is shown in Fig. 29.

Fabrication and characterization of of PbSe nanoparticles:

We have developed a laser-assisted spray process to deposit polymer films with embedded QDs. In this report we present results from two studies conducted to grow crystalline PbSe nanoparticles and uniform polymer films:

(1) Development of a chemical technique to grow crystalline PbSe nanoparticles in the size range of 5-10 nm with a narrow size distribution.

(2) Deposition of films of the semiconducting polymer P3HT with optical absorption properties that are similar to bulk.

We have developed a method to grow surfactant-coated PbSe QDs with a narrow particle size distribution. The particle sizes are controlled by the time of reaction. Low-resolution TEM image of PbSe QDs grown by this method is shown in Fig. 30. QDs were self-assembled on a carbon-coated TEM grid. Optical properties of these QDs were investigated by absorption spectroscopy and Photoluminescence (PL) spectroscopy. Absorption corresponding to 1st, 2nd and 3rd quantum levels of three different particle sizes are shown in Figs. 31 & 32. PL measurement presented in Fig. 32 also confirms the 0.65 eV band gap of the QD.

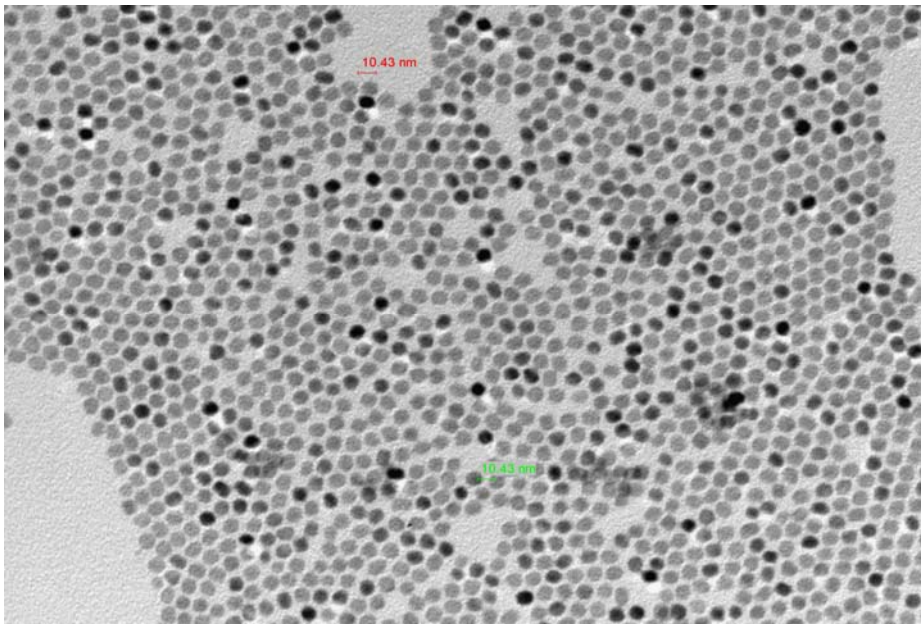

Fig. 30: TEM image of PbSe nanoparticles self-assembled on a carbon coated TEM grid.

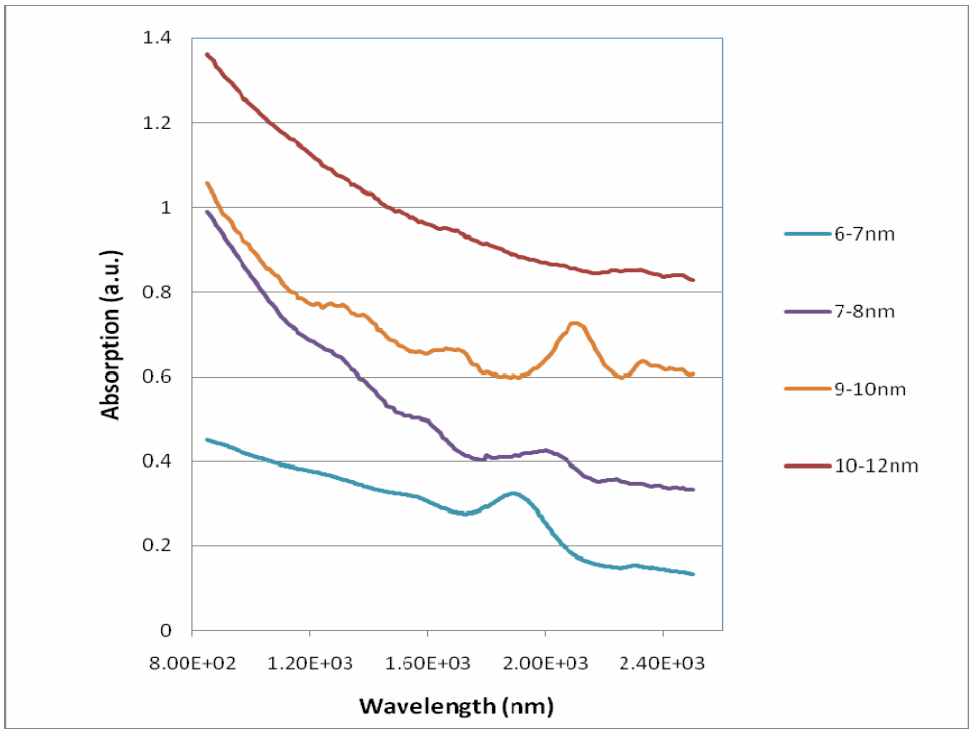

Fig. 31: Optical absorption by PbSe nanoparticles with different diameters that demonstrate quantum confinement.

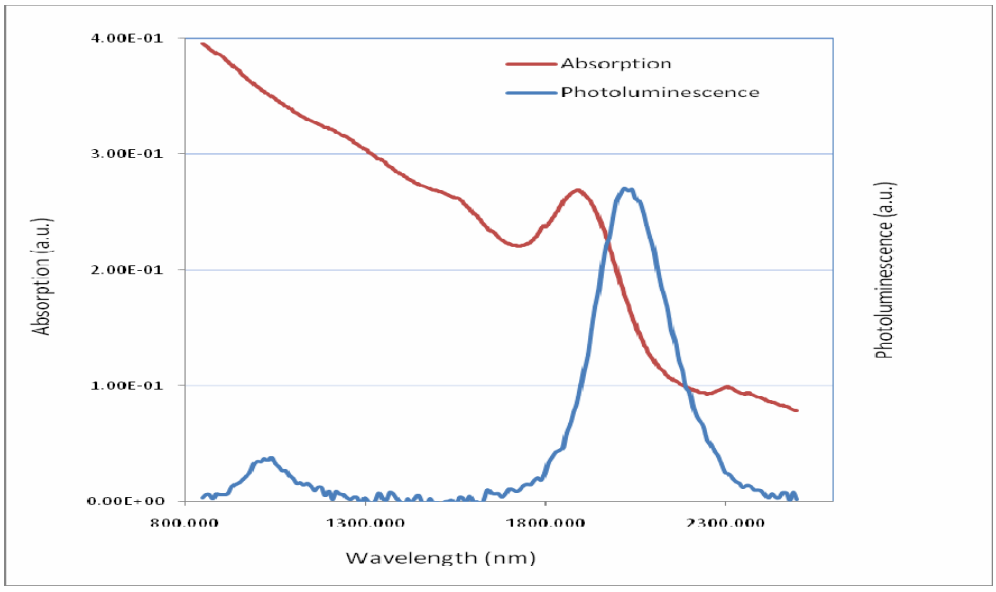

Fig. 32: Photoluminescence and absorption in PbSe nanoparticles with diameters in the rage of 9-10 nm.

Growth and characterization of surfactant-free PbSe nanoparticle films:

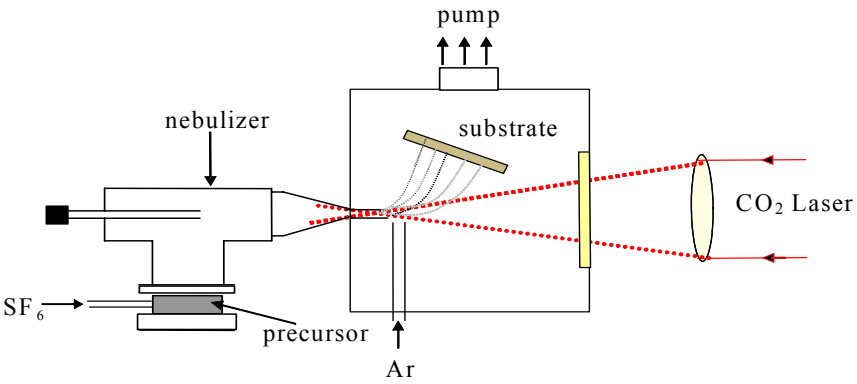

Fig. 33: Laser-assisted spray pyrolysis system for nanoparticle growth.

The first phase of the project involved the deposition of PbSe QDs on a substrate with particle sizes in the range of 6-10 nm. We have used a colloidal technique to grow PbSe nanoparticle suspensions in toluene. These particles are stabilized with surfactants. The nanoparticle solution is used in a Laser-Assisted Spray (LAS) process to deposit nanoparticles on a substrate. In this method for nanoparticle growth a CO_2 laser with a wavelength of 10.6 μm is used to heat a carrier gas that has a high absorption at that wavelength to create a high-temperature zone. The schematic diagram of the experimental apparatus is shown in Fig. 33. The nebulizer forms a mist that contains droplets of the solvent with a mean diameter of about 1.5 μm. The aerosol is injected into the growth chamber through a nozzle by the carrier gas sulfur hexafluoride (SF_6). A 3-5W cw CO_2 laser beam of wavelength 10.6 μm is focused to a point just inside the nozzle and is resonantly absorbed into the SF_6 molecules through vibrational excitation. Therefore, the carrier gas is heated by the CO_2 laser as the aerosol/gas mixture passes through the nozzle. Under optimum conditions, gas temperatures as high as 500^{o}C have been observed. The laser energy is adjusted to control the temperature of the gas so that the solvent in a drop is completely evaporated. The high temperature also evaporates any surfactants on the particle surfaces. However, the temperature should be low enough not to cause fusion of particles. Nanoparticles are diverted on to the substrate by an inert gas jet, as shown in Fig. 33.

We have successfully used the LAS process to grow PbSe nanoparticles on substrates. Transmission Electron Microscopy (TEM) images of a self-assembled layer of PbSe QDs formed by drop-casting from a PbSe QD/heptane solution are shown in Fig. 34 (a). As observed the surfactants caused the particles to be separated by a few nanometers. Fig. 34 (b) shows low-resolution TEM image of a uniformly distributed QD layer and a high-resolution TEM image of adjacent PbSe QDs in a film deposited by the LAS process.

Clearly the surfactants have been removed in the LAS process to form intimate contacts between adjacent QDs while the identity of each QD is maintained. Fig. 35 shows an absorption spectrum comparing the absorption by as-grown surfactant-coated PbSe QDs in a heptane solution to that from a nanoparticle film deposited by the LASP. Indications of the 1st, 2nd and 3rd quantum levels are visible in both solution and film. Intensities are low for the film as the absorption depth is significantly lower than that for the QDs in a solution.

This demonstrates that the LAS method can uniformly coat a surface with PbSe QDs without altering the quantized energy levels in QDs. We have also used the LAS method to deposit P3HT polymer films from a solution of P3HT dissolved in heptane. As shown in Fig. 36,

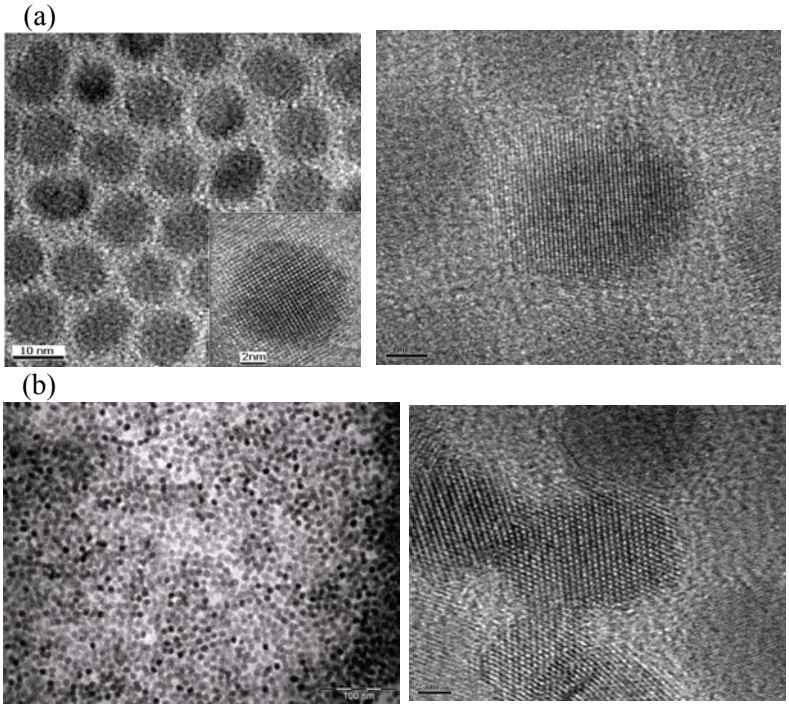

Fig. 34: Low and high resolution TEM images of a (a) self-assembled PbSe QDs with surfactants, (b) low and high resolution TEM image of PbSe QD films deposited by LAS.

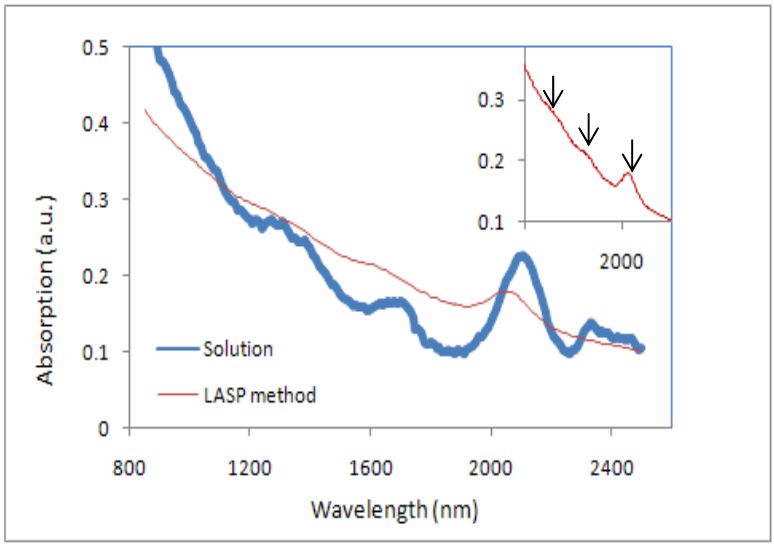

Fig. 35: Absorption spectra of 10.9nm quantum dots in solution and after LASP deposition. Inset: Absorption spectrum of LASP nano-film.

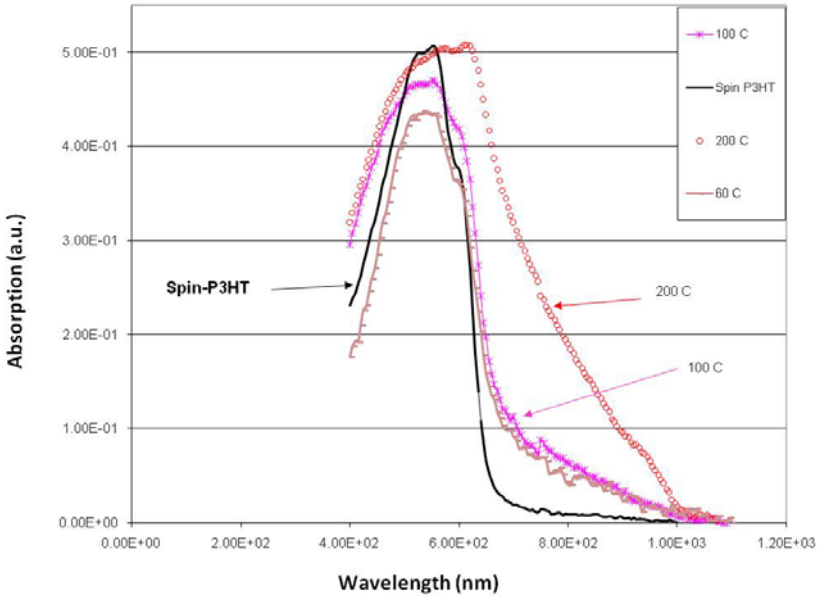

Fig. 36: Optical absorption by P3HT polymer films fabricated at different substrate temperatures.

the absorption spectrum of these films grown under optimum conditions (growth temperature of 100^{o}C) matched that of a film fabricated by spin-coating on a substrate.

In summary, in this project we have developed a method to fabricate crystalline PbSe quantum dots in a volatile solvent with a narrow particle size distribution. Optical absorption and PL studies confirmed the quantum confinement characteristics of the QDs. We have used a laser-assisted spray process to deposit the PbSe QDs from the solution onto a substrate. QDs form a connected network while maintaining single crystal nature and thus the quantum confinement. This was demonstrated by optical absorption and PL spectroscopy. In addition, we have also produced films of the semiconducting polymer P3HT using the laser-assisted spray process. These films possessed the desired optical properties.

Task III: Solid-state materials for power conversion and refrigeration

Project 7 – High Performance nanofabricated thermoelectric materials for power generation

The controlled fabrication of nanoscale semiconductors with enhanced physical properties is a current goal of technical as well as fundamental interest. To this end, the influence of semiconductor grain boundaries on carrier transport becomes increasingly important in nanoscale polycrystalline systems, where surface, point defect, dislocation, and interfacial energy barrier scatterings can dominate the transport [46,48]. Recent identification of several higher efficiency thermoelectric (TE) materials can be attributed to nanoscale enhancement [49-56]. These materials demonstrate increased Seebeck coefficient and decreased thermal conductivity due to the phenomenological properties of nanometer length scales, including enhanced interfacial phonon scattering and charge carrier filtering. Nanostructured TE enhancement aims to 'split' the interdependence of the electrical and thermal transport, allowing for better optimization of the TE figure of merit, $ZT = S^2T/\rho\kappa$ [57]. This equation defines the effectiveness of a material for TE applications, where S is the Seebeck coefficient, T is the absolute temperature, ρ is the electrical resistivity, and κ is the thermal conductivity. The reduction of κ through the interface scattering of phonons remains the primary mechanism for increased TE performance in nanostructured systems [44, 46-48]. However, to achieve superior TE performance requires enhancement of the power factor (S^2/ρ). Carrier filtering, where the presence of interfacial energy barriers filters low energy charge carriers traversing the interface, has been theoretically predicted [58, 59]. This increases $|S|$, as its value depends on the mean carrier energy relative to the Fermi level [57]. An understanding of this phenomenon in bulk materials is of fundamental importance. A small body of work has indicated that TE property improvements for bulk nanocrystalline materials are feasible [60-62], however, the physical mechanism responsible for S enhancement in these materials has not been developed.

To this end, we have begun an investigation into the transport properties of doped and undoped nanocomposites, i.e. nanocrystals densified within a macro-scale nanocomposite. In parallel to this experimental investigation, a theoretical study was also undertaken. We propose a phenomenological model to describe the diffusion transport of carriers through a material composed of nanogranular regions. The material is viewed as containing potential interface barriers due to the grains, and the transport includes quantum transmission and reflection from those barriers. Additional scattering mechanisms, such as carriers/acoustic phonons, carriers/non-polar optical phonons, and carriers/ionized impurities, which are relevant for thermoelectric materials, are also taken into account. The model can describe experimental data for PbTe nanocomposites but can also be used to calculate carrier transport properties of polycrystalline materials in general. It involves a set of physical parameters which can be measured independently or taken from the literature, to model experimental data or make predictions for other TE materials. In general, the model allows one to determine the importance of the barrier scattering mechanism as compared to the other relevant mechanisms.

A. Experimental Results and Discussion

PbTe nanocomposites were prepared by densifying 100 nm PbTe nanocrystals synthesized in high-yield employing a solution-phase reaction of two monometallic aqueous

precursor solutions [62, 63]. The carrier concentrations were modified by directly doping the PbTe nanocrystals with Ag (Ag_2Te) prior to the densification procedure (specimens III and IV). Spark Plasma Sintering (SPS) successfully consolidated these nanoscale grains within a dense PbTe matrix at 95 % bulk theoretical density. Densifying solely the nanocrystals results in the dispersion of non-conglomerated nanostructure within a bulk matrix, with grains ranging from 100 nm to over 1 micron, as shown in Fig. 37. Table I lists room temperature physical properties, described below. X-ray diffraction following SPS indicated ~ 5 vol. % $PbTeO_3$ impurity for specimens I and II, and ~ 3 vol. % Te_4O_9 impurity for specimens III and IV.

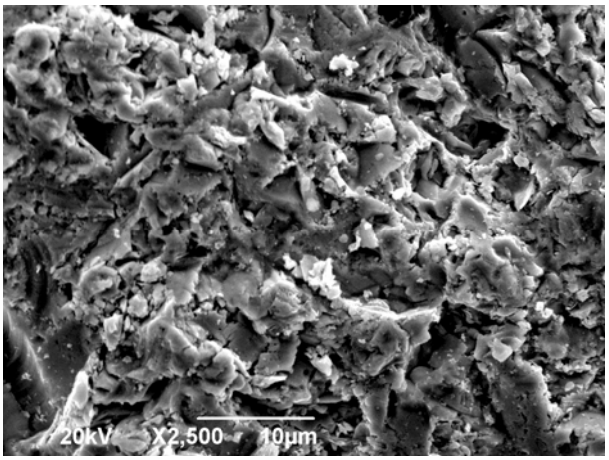

Fig. 37: Representative SEM micrograph of a specimen III fracture surface indicating 100 nm to over 1 micron grains distributed within a bulk material.

Table 3. Room temperature thermal conductivity κ, resistivity ρ, Seebeck coefficient S, carrier concentration p, energy barrier height E_B, trapping state density N_t, energy barrier width W, and effective crystallite size L, at 300 K, for undoped PbTe (specimens I and II) and Ag-doped PbTe (specimens III and IV).

Specimen	κ ($W\text{-}m^{-1}K^{-1}$)	ρ ($m\Omega\text{-}cm$)	S ($\mu V/K$)	p (cm^{-3})	E_B (meV)	N_t (cm^{-2})	W (nm)	L (nm)
I	2.2	24.9	328	9.5×10^{17}	60	1.0×10^{13}	54	316
II	2.5	12.6	324	1.5×10^{18}	60	1.3×10^{13}	43	396
III	2.8	3.9	198	5.1×10^{18}	60	2.4×10^{13}	23	376
IV	2.7	2.9	207	6.2×10^{18}	60	2.6×10^{13}	21	416

The nanocomposites were cut into 2 x 2 x 5 mm^3 parallelepipeds for transport property measurements. Four-probe ρ and S were measured from 12 to 300 K in a custom radiation-shielded vacuum probe with maximum uncertainties of 4 %, and 6 %, respectively, at 300 K [64]. Temperature dependent four-probe Hall measurements were conducted from 5 to 300 K at both positive and negative magnetic fields of up to 5 T to eliminate voltage probe misalignment effects.

For all specimens, a linear and positive magnetic field dependence of the Hall resistance confirms dominant p-type conduction. The carrier concentrations increase upon Ag-doping by more than a factor of 5, as listed in Table 3. Correspondingly, the ρ values, as shown in Fig. 38, exhibit a significant reduction in magnitude compared to the undoped specimens. All specimens

exhibit relatively large room temperature *S* values of approximately 325 μV/K for the two undoped specimens and 200 μV/K for the two Ag-doped specimens.

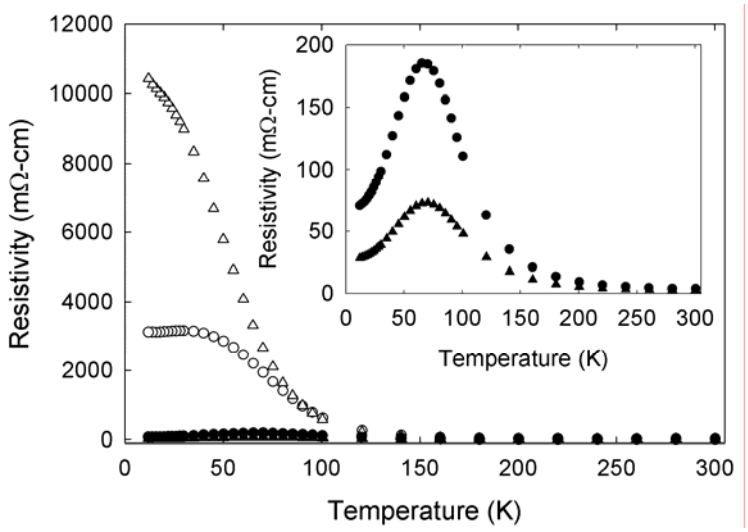

Fig. 38: Temperature dependence of the resistivity for specimens I (○), II (△), III (●), and VI (▲).

The low temperature ρ values show activated temperature dependence ($d\rho/dT < 0$) in all specimens, and a nonlinear increase with decreasing temperature but with a sharp peak in ρ near 70 K for the Ag-doped specimens (Fig. 38). Below 70 K the ρ values rapidly decrease with decreasing temperature. However, temperature dependent carrier concentration for all specimens indicates only a weak dependence with temperature. Lead chalcogenides exhibit large dielectric permittivity (ε) and small effective mass (m^*) that merge impurity levels with the allowed energy bands [65, 66]. The large ε results in low temperature impurity ionization, with energy $\propto m^*\varepsilon^{-2}$ [67] and consequently, a carrier concentration independent of temperature where there is no degeneracy.

Figure 39 shows the temperature dependence of the mobility, μ, for the two Ag-doped specimens in comparison to the two undoped nancomposites. While the room temperature mobilities are consistent with those reported in the literature, the temperature dependence differs significantly from single crystal and polycrystalline lead chalcogenides since the nanocomposite mobilities decrease with decreasing temperature, opposite to that of bulk materials reported in the literature [65-69]. In addition, the low temperature μ values for the Ag-doped specimens also show an order of magnitude increase as compared to the undoped specimens and exhibit a dramatic dip in μ (an approximately twenty-fold decrease) near 80 K, as compared to those values at the lowest temperature.

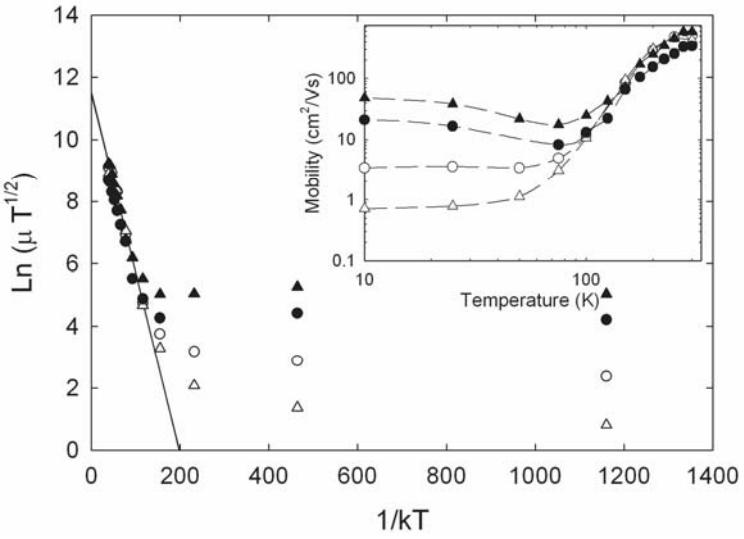

Fig. 39: Temperature dependence of the mobility for specimens I (○), II (△), III (●), and VI (▲). Lines are a guide for the eye only. Plotting the logarithm of $\mu_{eff} = \mu_o (1/T)^{1/2} \exp(-E_B/kT)$ and fitting the high temperature data yields an energy barrier of 60 meV for all specimens.

The scattering mechanisms that dominate the transport in bulk lead chalcogenides do not fully describe the unique temperature dependence of μ in these nanocomposites, implying the presence of an additional scattering mechanism. In nondegenerate semiconductors the carriers are scattered by long-wavelength acoustic phonons, $\mu \propto m^{*-5/2} T^{-3/2}$[65]. Since m^* is inversely proportional to temperature in lead chalcogenides, the mobility therefore varies with $T^{-5/2}$, as experimentally observed in single crystal and polycrystalline lead chalcogenides, with a weaker dependence in degenerate specimens [65, 66]. This dependence is opposite of that observed in the PbTe nanocomposites, suggesting phonon scattering is present in combination with an additional mechanism. Furthermore, the decreasing μ with decreasing temperature in these nanocomposites may suggest large impurity scattering of the carriers, where $\mu \propto T^{3/2}$. However, the high ε in PbTe implies suppression of long-range Coulomb potentials, limiting scattering to near the internal point of an impurity due to the large Bohr radius ($\propto m^{*-1}\varepsilon$, on the order of the lattice constant) [70] and consequently, a small screening length. This indicates scattering by ionized impurities is not a dominant mechanism in this material, particularly at room temperature where the interaction time (the time required for the carrier to pass the region of one impurity ion) [71] is significantly shorter. Consequently, μ is not proportional to $T^{3/2}$ in these nanocomposites.

The nanocomposite carrier conduction can be effectively described as dominated by grain-boundary potential barrier scattering, in combination with phonon scattering. Similar models have successfully described the electrical properties of silicon, CdTe, and nanostructured metal oxide films [48, 72-74]. Our previous work indicated oxygen adsorption in the PbTe nanocomposites [62]. This surface reactivity is difficult to prevent, considering the aqueous nature of the synthesis technique [62, 63]. The surface oxidation of PbTe is a sequential process, proceeding first through the formation of weak peroxide-like structures (up to 70 % coverage)

then by the chemisorption of oxygen [75]. Density Functional Theory (DFT) calculations of the surface reactivity of PbTe [75] indicate these oxygen complexes form chemical bonds by transferring charge from the tellurium atoms [75]. These chemical shifts were experimentally confirmed through X-ray Photoemission Spectroscopy (XPS) [75]. The chemisorption of oxygen essentially forms carrier trapping acceptor states by removing electrons from the grain surface, reducing itinerant carrier density. For nanocrystalline materials, this chemisorption results in increased trapping of carriers at grain boundaries, forming energy barriers that impede the conduction of carriers between grains. Assuming a uniformly distributed concentration of ionized carrier traps, N_t /cm^2, a grain boundary thickness less than the crystallite size L, whose morphology and size distribution are identical, and ρ within the grains less than through the boundary, the effective mobility is given by [72]:

$$\mu_{eff} = Lq\left(\frac{1}{2\pi m^* kT}\right)^{1/2} \exp\left(-\frac{E_B}{kT}\right), \tag{1}$$

where q is the carrier charge, m^* the effective mass, k the Boltzmann constant, T the temperature, and E_B is the height of the energy barrier in the depletion region. A plot of the logarithm of μ with $1/kT$ for the PbTe nanocomposites indicates activated behavior from conduction through the boundary potential barrier between grains (Fig. 38). Fitting the higher temperature data yields an energy barrier E_B = 60 meV for all specimens. This suggests the energy barriers form through a similar oxygen chemisorption mechanism in both the undoped and Ag-doped specimens. Conduction through ballistic transport occurs when the average energy of the charge carriers is sufficient to overcome this energy barrier. As the temperature increases, the average energy of the charge carriers increases and therefore the electrical conductivity increases $\propto T^{-1/2}\exp(-E_B/kT)$. This mechanism dominates at higher temperature and for higher carrier densities, where the concentration of carriers with larger average energy is larger. However, an additional conduction mechanism dominates at lower temperature. When the grain boundary energy barrier is sufficiently narrow and high, the charge carriers quantum mechanically tunnel through the barrier (thermionic field emission) [72]. In equilibrium, the dependence of barrier height E_B on the density of trapping states N_t and the carrier concentration p is given by [48, 73]: $E_B = q^2 N_t^2 / 8\varepsilon\varepsilon_o p$, and the barrier width (space charge region) by: $W = \left(2\varepsilon\varepsilon_o E_B / q^2 p\right)^{1/2}$, where q is the carrier charge, ε = 414 for PbTe at 300 K [76], and ε_o is the vacuum permittivity. Table I lists these calculated values for the two undoped specimens in comparison to the two Ag-doped specimens. As the carrier concentration increases with doping, the barrier height remains constant, but promotes an increase in trapping state density. Furthermore, as the carrier concentration increases, the barrier width decreases by a factor $\propto p^{-1/2}$. This suggests an increase in tunneling conduction (transmission probability) with doping.

The one-dimensional, time-independent WKB transmission probability τ for the potential barrier is given by [77]:

$$\tau(E) = \exp\left(-2\int_{x_1}^{x_2} \left\{2m^*\left[qV(x) - E\right]\right\}^{1/2} dx/\hbar\right), \tag{2}$$

where x_1 and x_2 are the classical carrier turning points with energy E, m^* is the effective mass, and $qV(x)$ is the interfacial barrier energy. Therefore, the tunneling probability is a maximum for

charge carriers with smaller m^*. The electrical transport in p-type PbTe is dominated by two bands: a lower mobility heavy hole (HH) valence band below the light hole (LH) valence band at low temperature, where $m_{LH}^* \sim 10\ m_{HH}^*$ [65, 78]. We assume similar m^* and band structure for the nanocomposites, as shown in Figure 4. At low temperature and higher hole densities, the electrical properties are dominated nearly exclusively by the LH carriers. As the temperature increases, the HH band rises, resulting in a decreasing τ and an increase in carrier scattering for the higher carrier density specimens. At higher temperature, when the average energy of the charge carriers is sufficient to overcome the grain boundary energy barrier, conduction is dominated through thermionic emission, $T^{1/2}\exp(-E_B/kT)$, and μ increases with temperature. Grain-boundary potential barrier scattering of the carriers, in combination with phonon scattering, gives rise to the unique temperature dependence of the electrical conductivity and the mobility in these nanocomposites.

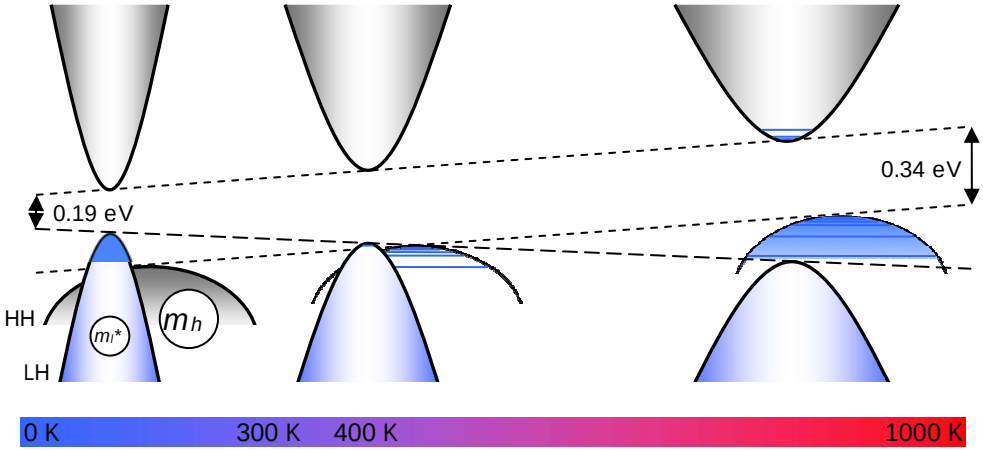

Fig. 40: Temperature dependence of the conduction and valence bands of PbTe.[20]

The effective crystallite size was estimated using Equation 1, the energy barriers obtained from fitting the temperature dependence of μ, the μ values calculated from the room temperature carrier concentration, and the HH $m^* = 1.5m_o$ [65]. These estimates indicate effective crystallite sizes between 300 and 400 nm, listed in Table I, and are consistent with the dimensional nanocomposite structure observed in our SEM analyses. This suggests the grain boundary energy barrier scattering is dominated through these nanoscale features. We note that inclusion of LH carriers in the calculation would only slightly lower the effective crystallite size.

Furthermore, conduction through the boundary potential barrier between grains essentially filters lower energy charge carriers, increasing the average carrier energy and consequently, $|S|$. Fig. 41 shows the room temperature S for the PbTe nanocomposites in comparison to theoretically calculated bulk values [65, 79], indicating an enhancement in S as compared to bulk PbTe at the same carrier concentration. In addition, we compare the room temperature S^2/ρ for the nanocomposites to two of our undoped and two Na-doped bulk PbTe specimens, indicating an enhancement in S^2/ρ over that of bulk PbTe (inset in Fig. 41). The larger S^2/ρ in the nanocomposites as compared to bulk polycrystalline materials, in addition to similar thermal conductivities (Table 3 and Ref. 65), results in enhanced room temperature ZT as

compare to bulk PbTe. This suggests interfacial energy barrier carrier filtering may be an effective method of thermoelectric performance enhancement in these bulk nanocomposites. Similar carrier filtering enhancements to *S* were observed in InGaAs/InGaAlAs heterostructures [80].

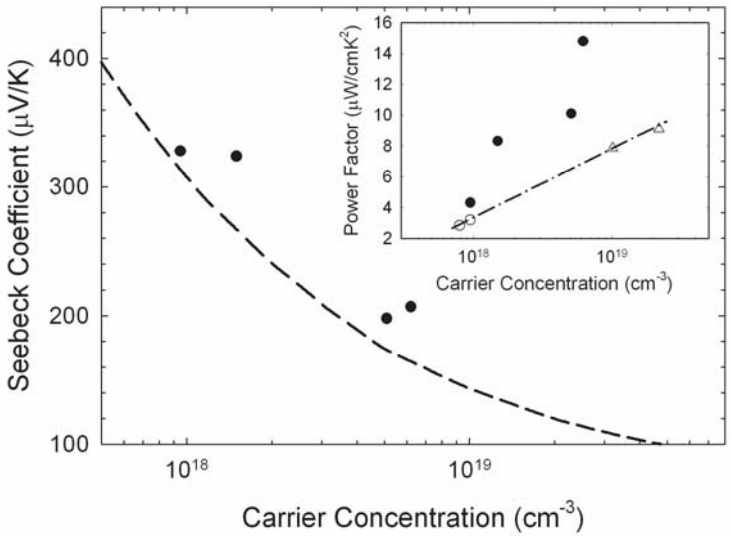

Fig. 41: Seebeck coefficient as a function of carrier concentration for the four PbTe nanocomposites (●) and the calculated bulk relationship (dashed line) from Ref. 79. Inset: Power Factor as a function of carrier concentration for the four PbTe nanocomposites in comparison to bulk undoped PbTe (○) and Na-doped PbTe (△). The straight line is a guide for the eye only.

In conclusion, PbTe nanocomposites were prepared by densifying 100 nm PbTe nanocrystals synthesized in high yield employing a solution-phase technique. SPS successfully consolidated these nanoscale grains within a dense PbTe matrix. The carrier concentrations were modified by directly doping the PbTe nanocrystals with Ag prior to densification. The unique temperature dependence of ρ and μ suggests an additional scattering mechanism in combination with phonon-carrier scattering dominant in single crystal and polycrystalline lead chalcogenides. In these nanocrystalline materials, the chemisorption of oxygen results in increased trapping of carriers at grain boundaries, forming energy barriers that impede the conduction of carriers between grains. This conduction can be effectively described as dominated by grain-boundary potential barrier scattering, in combination with phonon scattering. To our knowledge, this study represents the first bulk characterization of Ag-doped nanocrystals densified within a macro-scale nanocomposite. Furthermore, these nanocomposites demonstrate an enhanced TE performance as compared to bulk PbTe, suggesting interfacial energy barrier carrier scattering is an effective method of thermoelectric performance enhancement in bulk nanocomposites.

B. Theoretical Model

The proposed model for the description of the electronic transport characteristics is based on the well known expressions for σ and S defined as follows [41]:

$$\sigma = \frac{2e^2}{3m^*}\int_0^\infty \tau(E)g(E)E\left(-\frac{\partial f(E)}{\partial E}\right)dE\,, \tag{3}$$

$$S = \frac{1}{eT}\left[\frac{\int_0^\infty \tau(E)g(E)E^2\left(-\frac{\partial f(E)}{\partial E}\right)dE}{\int_0^\infty \tau(E)g(E)E\left(-\frac{\partial f(E)}{\partial E}\right)dE} - \mu\right] \tag{4}$$

where e is the electron charge, m^* is the effective mass, μ is the chemical potential for the specific material, $\tau(E)$ is the momentum relaxation time for the charge carriers, $g(E)$ is the total density of states (DOS) for the material, $f(E) = 1/(e^{(E-E_F)/k_BT}+1)$ is the Fermi distribution function with E_F being the Fermi level, and k_B is the Boltzmann constant. $\tau(E)$, $g(E)$, and $f(E)$ are energy-dependent functions but they also depend on other physical characteristics as defined for a specific material. Below we consider each of these functions individually and explain the relevant assumptions we make in our model.

Density of states

For PbTe the energy bands responsible for the transport are not parabolic. Their Fermi surfaces are ellipsoids of revolution. Using the two band Kane model, the energy dispersion is given as [65]

$$\frac{\hbar^2 k_l^2}{2m_l^*} + \frac{\hbar^2 k_t^2}{2m_t^*} = E + \alpha E^2 \tag{5}$$

where $k_{l,t}$ is the carrier momentum, $m_{l,t}^*$ is the effective mass along the longitudinal and transverse directions at the valence band minimum, respectively, and α is a non-parabolicity factor. For small band gap semiconductors, such as PbTe, $\alpha = 1/E_g$ where E_g is the energy gap. After defining an effective mass for both directions as $m^* = \beta^{2/3}(m_l^* m_t^{*2})^{1/3}$ (where β is the degeneracy of the Fermi surfaces containing more than one pocket), the total Density of States (DOS) for PbTe can be written as

$$g(E) = \frac{\sqrt{2}}{\pi^2}\left(\frac{m^*}{\hbar^2}\right)^{3/2}\sqrt{E(1+E/E_g)}(1+2E/E_g)\,, \tag{6}$$

$$E_g = E_g^0 + \gamma T \tag{7}$$

Here the variation of E_g as a function of temperature is also taken into account – $E_g^0 = 0.19eV$ is the PbTe band gap at $T = 0K$ and $\gamma \approx 0.0004eV/K$ is a phenomenological parameter for PbTe [82, 83].

Fermi distribution function

We further consider the Fermi distribution function. Although the expression is known, the Fermi distribution function contains an important parameter, the Fermi level E_F. E_F is specific for each material and is also related to the charge carrier concentration, *p*, via the expression [84]

$$p = \frac{4}{\sqrt{\pi}}\left(\frac{2\pi m^* k_B T}{h^2}\right)^{3/2}\int_0^\infty E^{1/2} f(E)dE \qquad (8)$$

where *h* is the Planck's constant. The self-consistent solution of the above equation allows one to determine the Fermi level E_F for a specific *p*.

Scattering mechanisms

Finally, we consider the momentum relaxation time, $\tau(E)$, with contributions from different scattering mechanisms. Here it is assumed that each scattering mechanism can be associated with a resistivity. Then the total relaxation time is obtained according to the Mathiessen's rule:

$$\frac{1}{\tau(E)} = \sum_i \frac{1}{\tau_i(E)} \qquad (9)$$

where $\tau_i(E)$ is the relaxation time for each contributing mechanism. For thermoelectric bulk materials, the carrier scattering may be due to acoustic phonons, non-polar optical phonons, or ionized impurities. For TE composites containing nanostructured grains, an additional scattering mechanism from the grain interfaces is also important.

In this model, the nanocomposite specimens is assumed to have grain regions with the same average characteristics. The grain interfaces in the material are modeled as rectangular potential barriers with an average height E_b, size *L*, and width *w*, as shown in Figure 6. The average values of E_b, *L*, and *w* can be inferred from experimental measurements [85, 86]. The physical explanation of the role of each boundary is that each grain boundary creates an interface density of traps Q_t [87, 88], which is assumed to be electrically neutral until carriers

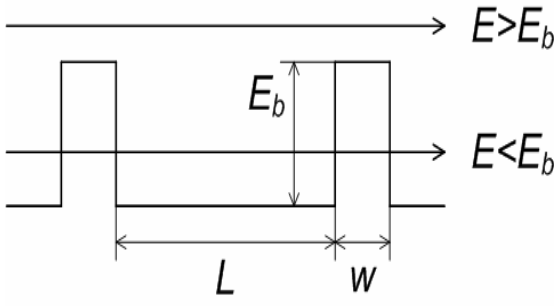

Fig. 42: Schematic drawing of a grain region limited by rectangular potential barriers. The height of the barrier is E_b, the width *w* and the grain size *L*. The carrier energy is *E*.

are trapped, thus creating a potential barrier with height E_b. The barrier height depends on L and p as $E_b = e^2 Q_t^2 / 8\varepsilon p$ where ε is the dielectric constant of the material. Also, if one considers that the barrier is formed by the complete filling of the traps, $w = Q_t / p$ [88].

As charge carriers diffuse through the sample, they can be reflected with a reflection coefficient, R, or transmitted with a transmission coefficient, T, quantum mechanically. The relaxation time due to this mechanism is then determined by the carrier mean free path, λ, and average velocity, v, of the carriers as follows:

$$\tau_b(E) = \frac{\lambda}{v}, \tag{10}$$

$$\lambda = \frac{L}{1-T}, \qquad v = \sqrt{\frac{2E}{m^*}} \tag{11}$$

where λ is assumed to be limited by scatterings from two neighboring barriers according to $\lambda = \frac{L}{1-T}$. Using the quantum mechanical expression for T [89], the relaxation time is:

$$\tau_b(E) = \begin{cases} L\sqrt{\dfrac{m^*}{2E}}\left[1 + \dfrac{4\dfrac{E}{E_b}\left(1-\dfrac{E}{E_b}\right)}{\sinh^2\left[\sqrt{\dfrac{2m^* E_b w^2}{\hbar^2}\left(1-\dfrac{E}{E_b}\right)}\right]}\right], E < E_b \\ L\sqrt{\dfrac{m^*}{2E}}\left[1 + \dfrac{4\dfrac{E}{E_b}\left(\dfrac{E}{E_b}-1\right)}{\sin^2\left[\sqrt{\dfrac{2m^* E_b w^2}{\hbar^2}\left(\dfrac{E}{E_b}-1\right)}\right]}\right], E > E_b \end{cases} \tag{12}$$

The relaxation times due to the other mechanisms can be expressed as:

$$\tau(E) = aE^s \tag{13}$$

where $s = -\frac{1}{2}, \frac{1}{2}, \frac{3}{4}$ for carrier scattering by acoustic phonons, non-polar optical phonons, and ionized impurities. The parameter a is temperature dependent. We use the expression for a for scattering by phonons. Since the impurity scattering contribution is much less significant for the experiments reported here, we do not consider it further. However, one can readily include this mechanism in the model using the relevant formulas in [66]. Thus

$$a_{a-ph} = \frac{h^4}{8\pi^3}\frac{\rho v_L^2}{k_B T}\frac{1}{(2m^*)^{3/2} D^2}, \qquad a_{o-ph} = \frac{h^2}{2^{1/2} m^{*1/2} e^2 k_B T(\varepsilon_\infty^{-1} - \varepsilon_0^{-1})} \tag{14}$$

where a_{a-ph} and a_{o-ph} are the constants for the acoustic and non-polar optical phonons, respectively, ρ is the mass density, v_L is the longitudinal velocity of sound, D is the deformation potential constant, ε_∞ is the high frequency dielectric constant, and ε_0 is the static dielectric constant. All of these variables can be taken from the available data in the literature or estimated experimentally for a particular specimen. The value for D is usually adjusted when phenomenological models are used to explain experimental measurements. However, *D* can also be estimated independently by measuring the changes in the material's E_g as a function of pressure and temperature [90].

C. Theoretical Results

The model described in the previous section provides all the necessary tools to calculate and explain the experimental data for σ and S for any small band gap TE material containing granular interfaces. The physical parameters and constants can be taken from available experimental data for a specific material or they can be measured independently for a particular specimen. The model can also be used to make predictions by varying one or several parameters characterizing the grain inclusions. Experiments involving such manipulations can be time consuming and expensive, thus this model can be used to steer and complement the experiments. Furthermore, it can be easily adapted to include additional features in the DOS (for example, a three band Kane model), additional scattering mechanisms, and two or one-dimensional transport.

Here we demonstrate that our model can be used to effectively describe experimental data for PbTe nanocomposite material. The model is

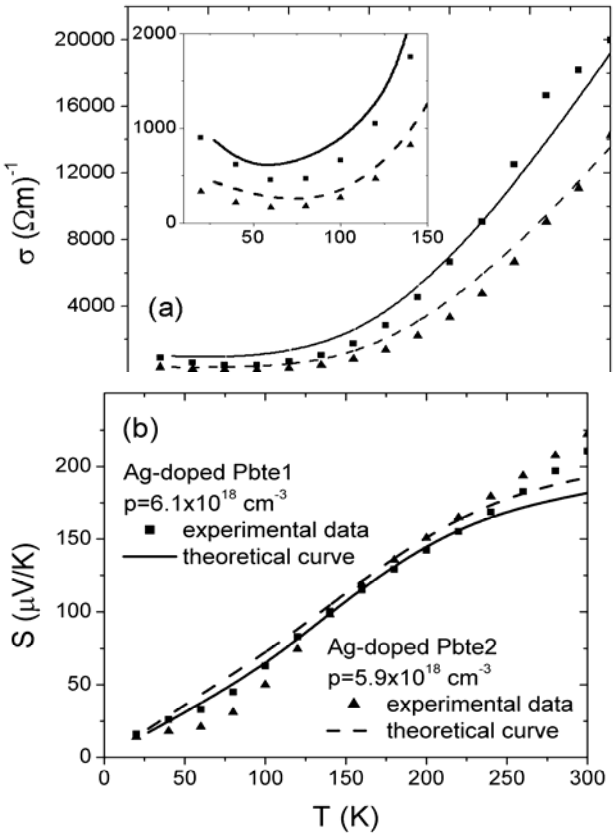

Fig. 43: Calculated and experimentally measured **(a)** electrical conductivity σ, and **(b)** Seebeck coefficient S as a function of the absolute temperature T for two values of the carrier concentrations.

tested by comparing to low temperature transport measurements for Ag-doped PbTe nanocomposites, synthesized and characterized as described above.

The experimental results for the carrier conductivity for two Ag-doped specimens with carrier concentration p = 6.1x10^{18} cm^{-3} and p = 5.9x10^{18} cm^{-3} are shown in Fig. 43(a). In Fig. 43(b), the experimental data S are also given. In addition, σ and S are calculated using Equations (3) and (4), and shown in Fig. 43(a) and 43(b), respectively. In our calculations, we used the barrier parameters estimated from the reported experimental data, described above, $E_b = 60meV$, $w = 50nm$, and $L = 300nm$. The rest of the parameters are taken as follows. The other parameters used are $m^* = 0.16m_0$, where m_0 is the electron mass [56], ρ = 8160 kg/m^3, v_L = 1730 m/s, and $\varepsilon_\infty^{-1} - \varepsilon_0^{-1} = 0.0072 \times E_g$ [81]. The value for D is varied in the range 5 – 15 eV range, as is usually done when phenomenological models are used to compare with experimental data [81]. As shown in Fig. 43, there is excellent agreement between the experimental results for the PbTe specimens and the model calculations in all temperature regions.

The model is further used to understand the importance of the different material characteristics that affect the transport properties. We investigate the role of carrier concentration on σ and S by changing p, and keeping all other parameters the same. The potential boundary characteristics are taken to be $E_b = 0.1eV$, $w = 50nm$, and $L = 300nm$, and the calculated results are shown in Fig. 44(a) and 44(b). The figures show that σ and S increase as a function of temperature. However, σ is larger for p due to the increased number of carriers, while S is larger for smaller p due to the higher mean energy per carrier.

The low temperature behavior of σ is similar to that of the experimental specimens, as shown in the inset in Fig. 43(a). As shown in Fig. 44(a), σ shows a minimum at $T \sim 70K$ for higher carrier concentrations. Another feature that one finds using this model is that the location of the σ minimum shifts toward larger T as p increases. We explain this by noting that at higher concentrations and temperatures, more carriers are excited above the barrier height, and the transmission probability through the barrier (Equation 12) also increases. Thus σ increases for larger temperatures. At lower temperatures, the majority of the charge carriers have energies less than the barrier height; therefore the conductivity can increase as there are more carriers available for tunneling. As a result of the interplay between these two relevant scattering mechanisms, σ exhibits a minimum at an intermediate temperature.

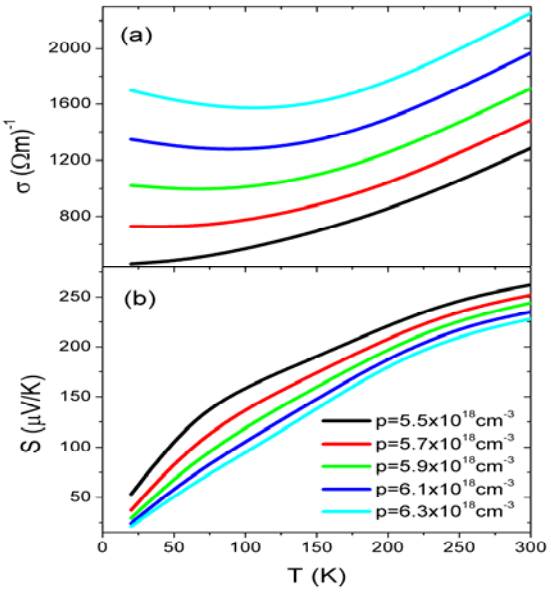

Fig. 44: (a) Electrical conductivity, σ, and (b) Seebeck coefficient, S, as a function of the absolute temperature T for different values of the carrier concentrations.

The model can also be used to determine how other parameters, related to the grain boundary specifications, affect the transport characteristics. Using Equations (3) and (4), one can calculate σ and S as a function of temperature for various barrier heights, barrier widths, and distances between the barriers. In Fig. 45, we show the calculated results for σ and S as a function of temperature for several values of the barrier height, while fixing the other barrier parameters to $w = 50nm$ and $L = 300nm$. The results from the model allows one to conclude that as E_b increases less carriers contribute to the transport in the specimen, thus leading to smaller σ, and larger S due to the larger mean energy per carrier.

We can achieve the same physical behavior by manipulating w or L. For example, increasing w results in a decrease in σ and an increase in S due to the smaller quantum mechanical transmission probability of the carriers through the barrier (Equations (12)). Furthermore, decreasing L results in a decrease in σ and an increase in S due to more frequent carrier scattering from the barriers. From Equations (3) and (4) the dependence of σ and S for various w and L show similar behavior as that described above.

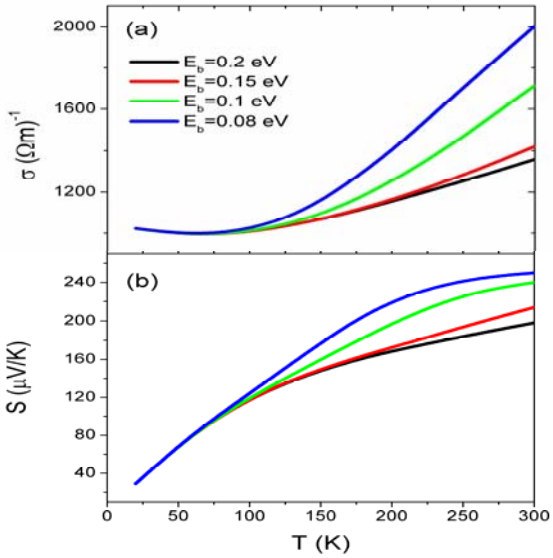

Fig. 45: (a) Electrical conductivity, σ, and (b) Seebeck coefficient, S, as a function of the absolute temperature T for different values of the potential barrier height.

In our phenomenological model several parameters characterizing the potential grain barriers can be adjusted in order to achieve a certain trend in the functional dependence of the carrier transport characteristics as a function of temperature. For thermoelectric applications, however, one is interested in increasing $S^2\sigma$. Thus the optimal E_b, w, and/or L are needed to optimize σ and S in order to achieve the highest performing TE materials. We therefore calculated $S^2\sigma$ using Equations (3) and (4) in

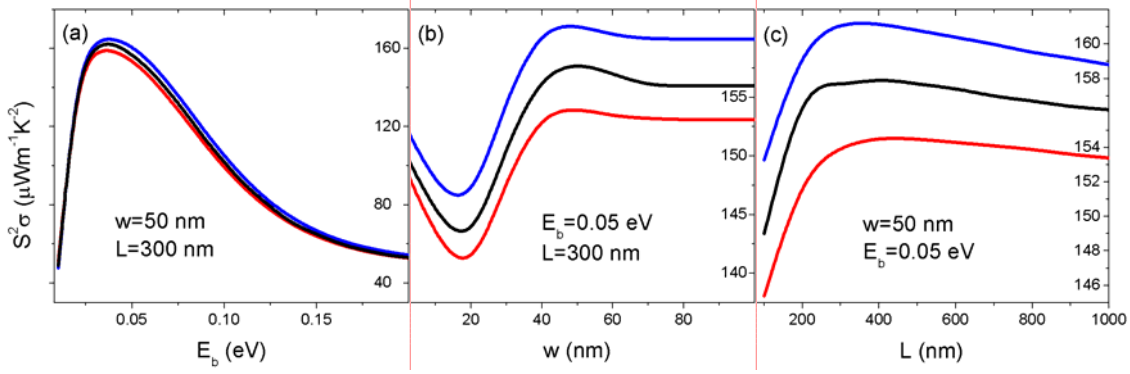

Fig. 46: Power factor as a function of **(a)** barrier height, **(b)** barrier width, and **(c)** grain size, at T=300 K. The carriers concentrations are p=5.7x10^{18} cm^{-3} (red line), p=5.9x10^{18} cm^{-3} (black line), and p=6.1x10^{18} cm^{-3} (blue line).

order to show how $S^2\sigma$ varies as a function of E_b, w, and L at a specific temperature. Our results are shown in Fig. 46. All parameter dependences show a maximum in $S^2\sigma$ vs. T, indicating the optimal parameters necessary in achieving the highest ZT values. It appears the highest $S^2\sigma$ for PbTe nanocomposites for the studied concentrations (shown in Fig. 45) can be achieved with $w \sim 50\,\text{nm}$, $L \sim 300\,\text{nm}$ and $E_b \sim 0.05\,\text{eV}$. We note that the existence of a maximum in $S^2\sigma$ is a consequence of the interplay between tunneling, reflectance, scattering from the barriers, and phonon scattering. In addition, the model described here, together with Figures 44-46, indicate that the carrier transport characteristics of a nano-polycrystalline material are not entirely independent. The mean energy per carrier can be affected by varying different grain characteristics. This will also have competing effects on S and σ. The reason for this is unambiguously related to the expressions for $\tau_i(E)$, DOS, and p. Our calculations show that it is possible to find a regime for which S increases but σ does not decrease substantially thus resulting in an overall increase in $S^2\sigma$. In fact, our model is one approach that directly shows how E_b, w, and L can be adjusted in such a way as to achieve the best TE performance for a given polycrystalline thermoelectric material.

A phenomenological model for describing the transport properties in nanocomposite materials was proposed and successfully applied to explain relevant experimental data. We model the TE material as consisting of nano-scaled granular regions with interfaces modeled as rectangular barriers. The transport through the material includes carrier quantum transmission and scattering from the barriers and carrier/phonon scattering within the grains. The theoretically calculated σ and S can reproduce the experimental observations obtained for Ag-doped PbTe and undoped PbTe nanocomposite specimens. We have shown that the interplay between the different scattering mechanisms, as well as the carrier concentration and the physical parameters for the barriers, is important in finding an optimal regime for optimizing a material's TE parameters. Specifically, our model reveals that by manipulating the barrier size and height, the mean energy per carrier can be increased leading to an increase in S without substantial degradation of σ. More importantly, this model can be adapted for other material systems by incorporating the relevant electronic structure parameters in the total density of states and scattering mechanisms.

III. Key Research Accomplishments

Some examples of research accomplishments and potential benefits are indicated below:

PROJECT SUCCESS	POTENTIAL MEDICAL / ARMY BENEFIT
Developed fundamental understanding of super-paramagnetism and underlying relaxation mechanisms (Brownian and Neel) of ferrofluids with varying particle sizes (10 to 20 nm) and different fluid viscosities to optimize ferrofluid properties (i.e. size distribution, carrier fluid characteristics etc.).	Hyperthermia and cell sorting applications
Novel magnetic nanotubes have been synthesized by embedding monodisperse magnetite nanoparticles into carbon nanotubes that are 100 nm wide and several microns long. These nanotubes will be horizontally dispersed on dielectric substrates.	The substrates will realize dual functional sensors (capacitance and magneto-impedance) that are chemically selective.
Composite Au-Fe3O4 nanoparticle structures based on core-shell, dumbbell-shaped and other geometric cluster configurations have been shown to yield novel and tailored magnetic properties such as tunable exchange bias along with surface plasmon resonance.	Nanomedicine applications –MRI contrast enhancement, targeted drug delivery
Developed nanocrystalline processing in high yield and fabrication of nanocomposites with high densification to achieve improved thermoelectric properties.	Power generation for Army medical equipment requiring lightweight portability, vibration-free operation, and high reliability. Also potentially useful for high individual soldier power density, waste heat recovery and all-electric DOD vehicular propulsion.
Characterized the effects of mechanical stress on viscoelastic parameters of cultured cells. Cellular responses to physical forces are very relevant to many basic functions including movement, proliferation, and development.	Cell growth rate in response to mechanical stimulation is the key factor for wound healing and tissue repair.
Developed techniques to uniformly embed PbSe quantum dots (QDs) in semiconducting polymers for enhanced charge transport between QDs and the polymer.	Important step towards the fabrication of light-weight flexible solar cells as a power source for electronic and medical instrumentation in remote locations.

IV. Reportable Outcomes

Publications and presentations based on support through grant USAMRMC W81XWH-07-1-0708 *(CIFM-supported researchers are shown in bold with PIs underlined):*

Published articles:

1. "Transverse susceptibility study of the effect of varying dipolar interactions on anisotropy peaks in a 3D assembly of soft ferrite nanoparticles" P. Poddar, **M. B. Morales**, N. A. Frey, S. A. Morrison, E. E. Carpenter and **H. Srikanth**, Journal of Applied Physics 104, 063901 (2008).
2. "Magnetoimpedance biosensor for Fe_3O_4 nanoparticles intracellular uptake evaluation" A. Kumar, V. Fal-Miyar, J. A. Garcia, A. Cerdeira, S. Mohapatra, **H. Srikanth**, J. Gass and G. V. Kurlyandskaya, Applied Physics Letters 91, 143902 (2007)
3. "Magnetoimpedance biosensor for Fe_3O_4 nanoparticles intracellular uptake evaluation" A. Kumar, V. Fal-Miyar, J. A. Garcia, A. Cerdeira, S. Mohapatra, **H. Srikanth**, *J. Gass* and G. V. Kurlyandskaya, Applied Physics Letters 91, 143902 (2007) (related publication)
4. "Bulk materials research for thermoelectric power generation applications" **G.S. Nolas**, **J. Martin**, M. Beekman and **X.N. Lin**, to appear in Mat. Res. Soc. Symp. Proc. Vol. 1064 (in press).
5. "Synthesis and thermoelectric properties of lead chalcogenide nanocomposites" **J. Martin**, S. Stefanoski, L. Chen and **G.S. Nolas**, , to appear in Mat. Res. Soc. Symp. Proc. Vol. 1044 (in press).
6. "Simple model of van der Waals interactions between two radially deformed single-wall carbon nanotubes", A. Popescu, **L.M. Woods**, and I.V. Bondarev, Phys. Rev. B **77**, 115443 (2008).

Submitted articles:

7. "Chemical synthesis and magnetic properties of cubic CoO nanocrystals and 3D nanostructures" V. Alexandrakis, G. Basina, D. Niarchos, G. Hadjipanayis, **S. Pal**, **H. Srikanth**, I. Panagiotopoulos, V. Tzitzios, J. Crystal Growth (under review 2008)
8. "Origin of magnetic anomalies in liquid, mixed and frozen states of ferrofluids" M. H. Phan, **M. B. Morales**, N. A. Frey and **H. Srikanth**, Nanotechnology (under review 2008)
9. "Anomalous magnetism and exchange bias in coupled Au-Fe_3O_4 nanoparticles" N. A. Frey, M. H. Phan, **H. Srikanth**, *S. Srinath*, C. Wang, S. Sun, Physical Review Letters (under review 2008)
10. "Synthesis and magnetic properties of gold-coated iron oxide nanoparticles" **S. Pal, M. B. Morales**, **P. Mukherjee** and **H. Srikanth**, Journal of Applied Physics (under review, 2008)
11. "Interparticle interactions in coupled Au-Fe_3O_4 nanoparticles" N. A. Frey, M. H. Phan, S. Srinath, C. Wang, S. Sun and **H. Srikanth**, Journal of Applied Physics (under review, 2008)

12. "Particle blocking and carrier fluid freezing effects on the magnetic properties of Fe_3O_4-based ferrofluids" **M. B. Morales**, M. H. Phan, **S. Pal**, N. A. Frey and **H. Srikanth**, Journal of Applied Physics (under review, 2008).
13. "Role of transition metal ions in the formation of an ohmic contact to silicon across the native SiO_2 layer", **S. Witanachchi**, H. Weerasingha, H. Abou Mourad, and **P. Mukherjee**, Physica B (submitted, 2008)
14. "A laser-assisted spray process for the growth of surfactant-free PbSe quantum dot films", **G. Dedigamuwa**, X. Jiang, J. Zhang, **P. Mukherjee**, and **S. Witanachchi**, Appl. Phys. Letts. (submitted, 2008)
15. "Intrinsic magnetic phases in cobalt ferrite thin films grown on silicon substrate by pulsed laser ablation", **T. Dhakal, D. Mukherjee**, **P. Mukherjee**, **S. Hariharan**, and **S. Witanachchi**, Appl. Phys. Letts. (submitted , 2008)
16. 'Enhanced Seebeck coefficient through energy barrier scattering in PbTe nanocomposites', **J. Martin**, L. Wang, L. Chen, and **G.S. Nolas** submitted to Physical Review B.
17. 'A model of transport properties of thermoelectric nanocomposite materials', A. Popescu, **L.M. Woods**, **J. Martin**, and **G.S. Nolas**, submitted to Physical Review B.
18. "Fabrication of organic solar array for applications in microelectromechanical systems" J. Lewis, **J. Zhang**, **X. Jiang**, Organic Electronics (submitted 2008)
19. "Chemical synthesis and magnetic properties of cubic CoO nanocrystals and 3D nanostructures" V. Alexandrakis, G. Basina, D. Niarchos, G. Hadjipanayis, **S. Pal**, **H. Srikanth,** I. Panagiotopoulos, V. Tzitzios, Small (submitted 2008)
20. "Enhanced Seebeck coefficient through energy barrier scattering in PbTe nanocomposites" **J. Martin**, L. Wang, L. Chen, J. Salvador, J. Yang and **G. S. Nolas**, Physical Review Letters, (submitted in 2008)
21. "Theoretical studies of anisotropic constitutive relationships in cyclotrimethylene trinitramine" M.W. Conroy, **I.I. Oleynik**, S.V. Zybin and C.T. White, Journal of Chemical Physics, (submitted, 2008)
22. "Anisotropic constitutive relationships in 1,3,5-triamino-2,4,6-trinitrobenzene (TATB)" - M.M. Budzevich, A. Landerville, M.W. Conroy, **I.I. Oleynik**, S.V. Zybin and C.T. White, Journal of Physical Chemistry A, (submitted 2008)
23. "First-principles reactive molecular dynamics study of initiation chemistry in PETN"- A. Landerville, M.A. Kozhushner, **I.I. Oleynik** and C.T. White, Journal of Chemical Physics, (submitted 2008)

Conference Presentations (invited/contributed):

1. "Magnetic properties of Fe_3O_4 and $CoFe_2O_4$ based ferrofluids" **M. B. Morales**, N. A. Frey, M. H. Phan and **H. Srikanth**, 52nd annual Magnetism and Magnetic Materials (MMM) conference, Tampa, FL (November 7 – 11, 2008)
2. "Transverse susceptibility probe of magnetic anisotropy and dipolar interactions in ferrite nanoparticles" **M. B. Morales**, N. A. Frey, P. Poddar and **H. Srikanth**, 2008 APS March meeting (New Orleans, LA)
3. "Surface and Interface magnetism in nanostructures and heterostructures" –Invited talk by **H. Srikanth** at the 2008 APS March meeting (New Orleans, LA)

4. "Interface magnetism in magnetic oxide nanostructures" Invited talk by **H. Srikanth** at the 2008 MRS Spring meeting (San Francisco, CA)
5. "Radio frequency transverse susceptibility in magnetic nanoparticles" **H. Srikanth**, **M. B. Morales**, N. A. Frey, P. Poddar, M. H. Phan, INTERMAG conference, May 4 – 8, 2008 (Madrid, Spain)
6. "Magnetism and magnetocaloric effect in ferrite and garnet nanoparticles" –Invited talk by **H. Srikanth** at the workshop on "Research trends in novel magnets for electromagnetic applications" –Santorini, Greece (Sep 2-5, 2008).
7. "Growth of nanoparticle coatings of $Ca_3Co_4O_9$ by a microwave plasma process" Ted Wangensteen, Marek Merlak, **Pritish Mukherjee**, and **Sarath Witanachchi**, International Conference on Thermoelectrics, August 3-7, 2008, Corvallis, Oregon.
8. "Growth and characterization of dual-laser deposited films of $Ba_8Ga_{16}Ge_{30}$ for thermoelectric applications", **R. Hyde**, **P. Mukherjee**, M. Beekman, **G. S. Nolas**, and **S. Witanachchi**, International Conference on Thermoelectrics, August 3-7, 2008, Corvallis, Oregon.
9. "Bulk Materials Research for Thermoelectric Power Generation Applications" - **G.S. Nolas, J. Martin**, M. Beekman and **X.N. Lin**, Invited, Materials Research Society Conference, Boston, MA, November 27, 2007.
10. "Transport Properties of Lead Chalcogenide Nanocomposites" - **G.S. Nolas**, **J. Martin**, S. Stefanoski, L. Wang and L. Chen, presented at the American Physical Society March Meeting, New Orleans, LA, March 13, 2008.
11. 'Structure-property Relationships in Skutterudites, Clathrates and Other Open-structured Materials', **G.S. Nolas**, Plenary Presentation, 27th International Conference on Thermoelectrics, Corvallis, OR, August 4, 2007.
12. "Transport Properties of Lead Chalcogenide Nanocomposites', **G.S. Nolas**, **J. Martin**, S. Stefanoski, L. Wang and L. Chen presented at the American Physical Society March Meeting, New Orleans, LA, March 13, 2008.
13. 'Enhanced Thermoelectric Properties of PbTe Nanocomposites', **J. Martin**, L. Wang, L. Chen and **G.S. Nolas**, presented at the 27th International Thermoelectrics Conference, Corvallis, OR, August 7, 2008.

Accepted conference presentations

14. "Origin of magnetic anomalies in the liquid, frozen and mixed states of ferrofluids" –M. H. Phan, **M. B. Morales**, N. A. Frey and **H. Srikanth** – poster to be presented at the 53rd annual MMM conference, Nov. 2008 (Austin, TX)
15. "Synthesis and magnetic properties of gold-coated core-shell $Au@Fe_3O_4$ nanoparticles" – **S. Pal, M. B. Morales**, M. H. Phan, **P. Mukherjee** and **H. Srikanth** –poster to be presented at the 53rd annual MMM conference, Nov. 2008 (Austin, TX).
16. "Anomalous magnetism and exchange bias in coupled $Au\text{-}Fe_3O_4$ nanoparticles" –N. A. Frey, M. H. Phan, S. Srinath, C. Wang, S. Sun and **H. Srikanth** –oral presentation to be given at the 2008 MRS Fall meeting, Dec. 2008 (Boston, MA)
17. "Functional magnetic nanostructures" –Invited talk to be given by **H. Srikanth** at the Magnetic Nanomaterials workshop in Kolkata, India (January 27-29, 2009).
18. "Growth of epitaxial $CoFe_2O_4$/PZT heterostructures and ferroelectric-ferromagnetic characterization", **D. Mukherjee, T. Dhakal, R. Hyde**, **P. Mukherjee**, **S. Hariharan**,

and **S. Witanachchi**, to be presented at 2008 Fall Materials Research Society Meeting, Boston, MA.

19. "A new method for forming surfactant-free PbSe quantum dot films and quantum dot-polymer composites for excitonic solar cells", **G. Dedigamuwa**, X. Jiang, J. Zhang, **P. Mukherjee** and **S. Witanachchi**,to be presented at 2008 Fall Materials Research Society Meeting, Boston, MA.
20. "Electronic structure of mechanically altered carbon nanotubes" - Y.V. Shtogun and **L.M. Woods**, Fourth International Multiscale Materials Modeling (MMM) Conference, October 27-31, 2008, (Tallahassee, FL)

V. Conclusion

Listed below are some accomplishments and corresponding future goals for the research work:

Accomplishments:

(1) Chemical synthesis and characterization of monodisperse magnetite nanoparticles (5 to 20 nm) as well as gold-coated core-shell nanoparticles
(2) Functionalization of multi-walled carbon nanotubes and rendering them magnetic by filling their bores with uniform dispersion of ferrofluids through novel capillary action method
(3) Process optimization to achieve high densification, void reduction, and improved electrical conductivity in the fabrication of thermoelectric nanocomposite materials
(4) Development of doped nanocrystals with enhanced thermoelectric properties
(5) Fabrication of epitaxial heterostructures of $CoFe_2O_4$ (ferromagnetic) and $Pb(ZrTi)O_3$ (ferroelectric) thin films for the development of multiferroic devices
(6) Fabrication of PbSe quantum dots (QDs) and p-type polymer films with required optical and electrical properties
(7) Demonstration of cellular viscoelasticity in response to static and cyclic stretching

Future Goals:

(1) Synthesis of water-based, biocompatible ferrofluids and ferro-gels
(2) Incorporation of magnetic nanomaterials into cells and tissue, and studying the DC and AC field response for cell sorting and hyperthermia applications
(3) Extension of the ferrofluid synthesis/characterization strategies to more viscous polymer gels/scaffolds for tissue engineering
(4) Investigation of thermal stability, theoretical modeling and subsequent predictive assessment of optimization of doped thermoelectrics
(5) Fabrication of $CoFe_2O_4$ nanopillars within $Pb(ZrTi)O_3$ films and investigation of multiferroic coupling in ZnO:V/ZnO:Mn heterostructures
(6) Formation of QD and p-type polymer hybrid structures for the development of flexible solar devices
(7) Fabrication of self-assembled polymer-coated gold nanotemplates for biological cell manipulation; study of cell growth and directional cell migration in response to mechanical force, with particular relationship to wound healing and tissue repair

Relevance of the Research:

From the perspective of military applications specific to the US Army Medical Research and the DoD in general, we have identified three key targeted applications where timely advances are critically needed. The concerted effort in this Integrated Functional Materials Project and our ongoing development of an interdisciplinary Center for Integrated Functional Materials (CIFM) at USF will advance the science knowledge base in these areas. The three targeted tasks broadly encompass issues of most importance to the soldier in the battlefield. At the culmination of the projects specific advances are expected in new materials and functionalities that aid in diagnostics and communication of medical problems encountered by the soldier in the field, sensors with improved sensitivity and specificity to detect threats such as trace biological agents,

and the need for novel portable and renewable energy and power sources to power these new devices.

Once established, CIFM will continue to be a national resource in the development of new materials and devices for the military and commercial sector, and a stimulant of industry in the United States based on emerging technologies and manufacturing processes. The specific outcome of the research activities is therefore expected to lead to new devices/systems/composite materials useful for the USAMRMC.

VI. Bibliography

(1) S. Odenbach, J. Phys.: Condens. Matter 16, R1135 (2004).
(2) W. Luo, S.R. Nagel, T.F. Rosenbaum, and R.E. Rosensweig, Phys. Rev. Lett. 67, 2721 (1991).
(3) Z. Wang and C. Holm, *Phys. Rev. E*, 68, 041401 (2003).
(4) A. Skumiel, A. Józefczak, T. Hornowski, and M Labowski, *J. Phys. D: Appl. Phys.*, 36, 3120-3124 (2003).
(5) M. Klokkenburg, B. H. Erne, and A. P. Philipse, *Langmuir*, 21, 1187-1191 (2005).
(6) W. Voit, D. K. Kim, W. Zapka, M. Muhammed, and K. V. Rao, *Mat. Res. Soc. Symp. Proc.*, 676, Y7.8 (2001).
(7) O.A. Valenzuela, J.M. Aquino, R.B. Galindo, O.R. Fernandez, P.C. Fannin, and A. T. Giannitsis, *J. Appl. Phys.*, 97, 10Q914 (2005).
(8) J. Zhang, C. Boyd, and W. Luo, Phys. Rev. Lett. 77, 390 (1996).
(9) L.Y. Zhang, Y.H. Dou, L. Zhang, and H.C. Gu, Chin. Phys. Lett. 24, 483 (2007).
(10) C.-M. Lo, J. Ferrier, "Electrically measuring viscoelastic parameters of adherent cell layers under controlled magnetic forces," *Eur. Biophys. J.* 28: 112-118 (1999).
(11) G. Korneva et.al, Nano Letters 5, 879-884 (2005).
(12) Z. L. Xiao et.al. Nano Letters 2, 1293 (2002).
(13) J.-C. Bradley; S. Babu , P. Ndungu; A. Nikitin; Y. Gogotsi, SMIRP Bradley Research Lab Knowledge Product 10975_0004, 27 (2003).
(14) V. Skumryev, S. Stoyanov, Y. Zhang, G. Hadjipanayis, D. Givord, and J. Nogués, Nature London 423, 850853, (2003).
(15) P. K. Gupta and C. T. Hung, Life Sci. 44, 175 (1989).
(16) S. Mornet, O. Lambert, E. Duguet, and A. Brisson, Nano Lett. 5, 281, (2005).
(17) C. Chouly, D. Pouliquen, L. Lucet, J. J. Jeune, and P. Jallet, J. Microencapsul. 13, 245, (1996).
(18) S. Mornet, S. Vasseur, F. Grasset, and E. Duguet, J. Mater. Chem. 14, 2161, 2004.
(19) D. K. Kim, M. Mikhaylova, Y. Zhang, and M. Muhammed, Chem. Mater. 15, 1617, 2003, and Refs. 4, 8, and 9 therein.
(20) E. X. Wu, H. Y. Tang, and J. H. Jensen, NMR Biomed. 17, 478, (2004).
(21) A. K. Gupta and A. S. G. Curtis, Biomaterials 25, 3029, (2004).
(22) F. Y. Cheng, C. H. Su, Y. S. Yang, C. S. Yeh, C. Y. Tsai, C. L. Wu, M. T. Wu, and D. B. Shieh, Biomaterials 26, 729, (2005).
(23) R. Weissleder, G. Elizondo, J. Wittenberg, C. A. Rabito, H. H. Bengele, and L. Josephson, Radiology 175, 489, (1990).
(24) T. A. Kent, M. J. Quast, B. J. Kaplan, R. S. Lifsey, and H. M. Eisenberg, Magn. Reson. Med. 13, 434 (1990).
(25) M. Tada, S. Hatanaka, H. Sanbonsugi, N. Matsushita, and M. Abe, J. Appl. Phys. 93, 7566 (2003).
(26) K. Nishimura, M. Hasegawa, Y. Ogura, T. Nishi, K. Kataoka, H. Handa, and M. Abe, J. Appl. Phys. 91, 8555 (2002).
(27) R. V. Mehta, R. V. Upadhyay, S. W. Charles, and C. N. Ramchand, Biotechnol. Tech. 11, 493 (1997).
(28) J. Lin, W. Zhou, A. Kumbhar, J. Wiemann, J. Fang, E. E. Carpenter, C. J. O'Connor, *J. Solid State Chem. 159*, 26 (2001).

(29) S. J. Cho, J. C. Idrobo, J. Olamit, K. Liu, N. D. Browning, S. M. Kauzlarich, *Chem. Mater*. *17*, 3181 (2005).
(30) M. Mikhaylova, D. K. Kim, N. Bobrysheva, M. Osmolowsky, V. Semenov, T. Tsakalatos, M. Muhammed, *Langmuir 20*, 2472 (2004).
(31) M. Mandal, S. Kundu, S. K. Ghosh, S. Panigrahi, T. K. Sau, S. M. Yusuf, T. Pal, *J. Colloid Interface Sci*. *286*, 187 (2005).
(32) J. L. Lyon, D. A. Fleming, M. B. Stone, P. Schiffer, M. E. Williams, *Nano Lett. 4*, 719 (2004).
(33) L. Y. Wang, J. Luo, Q. Fan, M. Suzuki, I. S. Suzuki, M. H. Engelhard, Y. H. Lin, N. Kim, J. Q. Wang, C. J. Zhong, *J. Phys. Chem. B 109*, 21593 (2005).
(34) L. Y. Wang, J. Luo, M. M. Maye, Q. Fan, Q. Rendeng, M. H. Engelhard, C. Wang, Y. H. Lin, C. J. Zhong, *J. Mater. Chem*. *15*, 1821 (2005).
(35) J. AM. CHEM. SOC. 126, 273-279 (2004).
(36) M.P.Morales, S. Veintemillas-Verdaguer, M. I. Montero, C. J. Serna, A. Roig, L. Casas, B. Martinez, F. Sandiumenge, Chem Mater. 11, 3058 (1999).
(37) W. Eerenstein, N. D. Mathur and J. F. Scott, Nature, 442, 759 (2006).
(38) A. M. J. G. Van Run, D. R. Terrell, and J. H. Scholing, J. Mater. Sci. 9, 1710 (1974).
(39) G. Srinivasan, et. al., Phys. Rev. B 65, 134402 (2002).
(40) L. Lian and N. R. Sottos, J. Appl. Phys 87, 3941 (2000).
(41) L. Horng, G. Chern, M. C. Chen, P. C. Kang, D. S. Lee, J. Magn. Magn. Mater. 207, 389 (2004).
(42) B. A. Gregg, J. Phys. Chem. B 107, 4688, (2003).
(43) B. A. Gregg, "Excitonic solar cells", J. Phys. Chem. B 107, 4688 (2003).
(44) R. D. Schaller and V. I. Kilmov, "High efficiency multiplication inPbSe nanocrystals: Implications for solar energy conversion, Phys. Rev. Lett. 92, 186601 (2004).
(45) W. Shockley and H. J. Queisser, "Detailed balance limit of efficiency in pn-junction solar cells", J. Appl. Phys. 32, 510 (1961).
(46) G. Blatter and F. Greuter, Phys. Rev. B 34, 8555 (1986).
(47) H. Marom, M. Ritterband, M. Eizenberg, Thin Solid Films 510, 62 (2006).
(48) C. H. Seager, J. Appl. Phys. 52, 3960 (1981).
(49) M. S. Dresselhaus, G. Chen, M. Y. Tang, R. Yang, H. Lee, D. Wang, Z. Ren, J. P. Fleurial, and P. Gogna, Adv. Mater. 19, 1043 (2007).
(50) L. D. Hicks, M. S. Dresselhaus, Phys. Rev. B 47, 16631 (1993).
(51) R. Venkatasubramanian, E. Siivola, T. Colpitts, B. O'Quinn, Nature 413, 597 (2001).
(52) T. C. Harman, P. J. Taylor, M. P. Walsh, and B. E. LaForge, Science 297, 2229 (2002).
(53) T. Kong, S. B. Cronin, M. S. Dresselhaus, Applied Physics Letters 77, 1490 (2000).
(54) J. P. Heremans, C. M. Thrush and D. T. Morelli, J. Appl. Phys. 98, 063703 (2005).
(55) K. F. Hsu, S. Loo, F. Guo, W. Chen, J. S. Dyck, C. Uher, T. Hogan, E. K.
(56) M. S. Dresselhaus, G. Chen, M. Y. Tang, R. G. Yang, H. Lee, D. Z. Wang, Z. F. Ren, J. P. Fleurial and P. Gogna, *Proc. Mater. Res. Soc.* 886 3 (2006).
(57) G. S. Nolas, J. Sharp, and H. J. Goldsmid, *Thermoelectrics: Basic Principles and New Materials Developments* (Springer, New York, NY, 2001).
(58) Y. I. Ravich, In *CRC Handbook of Thermoelectrics*, edited by D. M. Rowe, pages 67-73, CRC Press, New York, (1995).
(59) B. Moyzhes and V. Nemchinsky, Appl. Phy. Lett. 73, 1895 (1998).
(60) K. Kishimoto and T. Koyanagi, J. Appl. Phys. 92, 2544 (2002).

(61) J. P. Heremans, C. M. Thrush, and D. T. Morelli, Physical Review B 70, 115334 (2004).
(62) J. Martin, G. S. Nolas, W. Zhang, and L. Chen, Appl. Phys. Lett. 99, 222112 (2007).
(63) W. Zhang, L. Zhang, Y. Cheng, Z. Hui, X. Zhang, Y. Xie, and Y. Qian, Materials Research Bulletin 35, 2009 (2000).
(64) J. Martin, G. S. Nolas, H. Wang, and J. Yang, J. Appl. Phys. 102, 103719 (2007).
(65) Yu. I. Ravich, B. A. Efimova, and I. A. Smirnov, *Semiconducting Lead Chalcogenides,* Plenum, New York, p. 91 (1970) and references therein.
(66) W. Scanlon, in *Solid State Physics* 9, Academic Press, NY (1959).
(67) C. Kittel, Introduction to Solid State Physics, Second Edition, John Wiley & Sons, Inc., New York, p. 356 (1956).
(68) Z. H. Dughaish, Physica B, 322, 205 (2002).
(69) E. H. Putley, Proc. Phys. Soc. B 65, 388 (1952).
(70) E. H. Putley, Proc. Phys. Soc. B 65, 736 (1952).
(71) N. A. Poklonski, S. A. Vyrko, V. I. Yatskevich, and A. A. Kocherzhenko, J. Appl. Phys. 93, 9749 (2003).
(72) J. Y. W. Seto, J. Appl. Phys. 46, 5247 (1975).
(73) O. Vigil-Galan, Lıdice Vaillant, R. Mendoza-Perez, G. Contreras-Puente, J. Vidal-Larramendi, and A. Morales-Acevedo, J. Appl. Phys. 90, 3427 (2001).
(74) G. Kiriakidis, M. Suchea, S. Christoulakis, and N. Katsarakis, Rev. Adv. Mater. Sci. 10, 215 (2005).
(75) T. S. Zyubina, V. S. Neudachina, L. V. Yashina, V. I. Shtanov, Surface Science 574, 52 (2005).
(76) R. Clasen, G. Harbeke, A. Krost, F. Levy, O. Madelung, K. Maschke, G. Nimtz, B. Schlicht, F. J. Schmitte, and J. Treusch, *Landolt-Bornstein: Numerical Data and Functional Relationships in Science and Technology*, Volume 17 Semiconductors, Subvolume f, Ed. by K. H. Hellwege and O. Madelung, (Springer, New York, pg. 170, 1983).
(77) V. V. Miten, Phys. Rev. B 31, 2584 (1985).
(78) L. M. Rogers, Brit. *J. Appl. Phys.* 1, 1067 (1968).
(79) A. J. Crocker and L. M. Rogers, Brit. J. Appl. Phys. 18, 563 (1967).
(80) J. M. O. Zide, D. Vashaee, Z. X. Bian, G. Zeng, J. E. Bowers, A. Shakouri, and A. C. Gossard, *Phys. Rev. B* 74, 205335 (2006).
(81) D. M. Rowe and C. M. Bhandari, *Modern Thermoelectrics* (London, Holt Saunders, 1983)
(82) E. A. Albanesi, C. M. I. Okoye, C. O. Rodriguez, E. L. Peltzer y Blanca, and A. G. Petukhov, Phys. Rev. B 61, 16589 (2000)
(83) Z. Dashevsky, R. Kreizman, and M. P. Dariel, J. Appl. Phys. 98, 094309 (2005)
(84) A. K. Sreedhar and S. C. Gupta, Phys. Rev. B 5, 3160 (1972)
(85) K. Kishimoto and T. Koyanagi, J. Appl. Phys. 92, 2544 (2002)
(86) K. Kishimoto, K. Yamamoto, and T. Koyanagi, Jpn. J. Appl. Phys. 42, 501 (2003)
(87) R. E. Jones, Jr. and S. P. Wesolovski, J. Appl. Phys. 56, 1701 (1984)
(88) C. H. Seager, J. Appl. Phys. 52, 3960 (1981)
(89) N. Zettili, *Quantum Mechanics: Concepts and Applications* (John-Wiley, Chichester, 2001)
(90) C. M. Bhandari and D. M. Rowe, *Thermal Conduction in Semiconductors* (Wiley, New York, 1988)